Decoding MASLD Progression: A Molecular Trajectory-Based Framework for Modelling Disease Dynamics

Ioannis Kamzolas[1,4*], Thodoris Koutsandreas[1,2*], Charlie George Barker[1,3], Anna Vathrakokoili Pournara[1], Harry Weston[1,4], Naoto Fujiwara[5], Yujin Hoshida[6], Quentin M. Anstee[7,8], Michele Vacca[4,9], Irene Papatheodorou[1,10], Antonio Vidal-Puig[4,11 +], Evangelia Petsalaki[1+]

[1]European Molecular Biology Laboratory - European Bioinformatics Institute, Wellcome Genome Campus, Hinxton, CB10 1SD, UK

[2]Open Targets, Wellcome Genome Campus, Hinxton, CB10 1SD, UK

[3](current address) University College London Cancer Institute, London WC1E 6DD, UK

[4]MRC Institute of Metabolic Science, Metabolic Research Laboratories, University of Cambridge, Cambridge, UK

[5]Department of Gastroenterology and Hepatology, Mie University, 2-174 Edobashi, Tsu city, Mie 514-8507, Japan

[6]Division of Digestive and Liver Diseases, Department of Internal Medicine, Simmons Comprehensive Cancer Center, University of Texas Southwestern Medical Center, Dallas, Texas, USA.

[7]Translational & Clinical Research Institute, Faculty of Medical Sciences, Newcastle University, Newcastle upon Tyne, UK

[8]Newcastle NIHR Biomedical Research Centre, Newcastle upon Tyne Hospitals NHS Trust, Newcastle upon Tyne, UK

[9]Clinica Medica “Cesare Frugoni”, Interdisciplinary Department of Medicine, University of Bari ”Aldo Moro”, Bari, Italy; Roger Williams Institute of Liver Studies, School of Immunology & Microbial Sciences, Faculty of Life Sciences and Medicine, King’s College London, Foundation for Liver Research and King’s College Hospital, London, UK; National Institute for Biostructure and Biosystems (INBB), Rome, Italy.

28 [10](current address) Earlham Institute, Norwich Research Park, Colney Ln, Norwich NR4 7UZ

29 [11]Centro de Investigacion Principe Felipe, Valencia, Spain

30

31 + correspondence should be addressed to Antonio Vidal-Puig ajv22@medschl.cam.ac.uk and
32 Evangelia Petsalaki: petsalaki@ebi.ac.uk

33

34 * These authors contributed equally to the work presented in this manuscript

Abstract

Metabolic Dysfunction-Associated Steatotic Liver Disease (MASLD) has emerged as a silent pandemic, affecting nearly one-third of the global population. MASLD encompasses a spectrum of liver disorders, ranging from simple steatosis to Metabolic Dysfunction-Associated Steatohepatitis (MASH), characterised by lipotoxicity, hepatocellular injury, inflammation, and fibrosis, which can eventually progress to cirrhosis and hepatocellular carcinoma. Despite the progressive nature of MASLD/MASH, current research and clinical practice primarily rely on static, histopathology-defined stages that fail to capture the continuous nature of disease progression.

Here, we present an integrative framework that combines patient pseudo-temporal ordering, network analysis, and cell-type deconvolution to reconstruct the continuous MASLD/MASH trajectory. By analysing patient liver transcriptomic profiles, we position patients along this data-driven trajectory, moving beyond conventional stage-based classifications. This approach reveals the sequence of critical molecular events underlying MASLD/MASH progression, providing mechanistic insights into the disease's pathophysiology. By integrating these findings with plasma proteomics data, we identify novel trajectory-specific plasma biomarkers that predict disease stage (and trajectory position) independently of histology.

Together, these findings demonstrate the value of trajectory-based frameworks for understanding MASLD pathophysiology and highlight new opportunities for precision diagnosis and therapeutic target prioritisation across the disease spectrum.

Introduction

Metabolic Dysfunction-Associated Steatotic Liver Disease (MASLD) encompasses a spectrum of conditions, ranging from simple steatosis to Metabolic Dysfunction-Associated Steatohepatitis (MASH), which can progress to fibrosis, cirrhosis, and hepatocellular carcinoma[1]. This global epidemic affects nearly one-third of Western populations and is primarily driven by the rising prevalence of metabolic syndrome, type 2 diabetes, and obesity[2,3]. Despite its prevalence, most MASLD cases remain asymptomatic and undiagnosed until advanced stages.

Diagnosis of MASLD relies on imaging (ultrasound, MRI spectroscopy) and non-invasive fibrosis scores such as the NAFLD Fibrosis Score and FIB-4, developed initially to detect advanced fibrosis[4,5]. Although liver biopsy remains the histological gold standard, including for derivation of the NAFLD Activity Score[6], its use is limited by sampling variability and procedural risk[7,8]. Current AASLD and EASL–EASD–EASO guidelines endorse non-invasive tests but emphasise the need for complementary diagnostic strategies[9,10]. Elastography methods, including transient elastography (FibroScan)[11] and magnetic resonance elastography, have improved fibrosis assessment, but are limited by precision, accessibility, or cost. Consequently, despite improved histological scoring reproducibility[12], robust non-invasive biomarkers for MASLD remain lacking.

Advances in systems biology and multi-omics have accelerated MASLD/MASH research[13–17], with transcriptomic, proteomic, and metabolomic studies linking the disease to metabolic syndrome, insulin resistance, and processes such as lipid accumulation, ER stress, and oxidative stress[18]. Genome-wide association studies (GWAS) have identified major genetic risk factors, most notably the PNPLA3 I148M variant[19–21,22], which was later validated across large multi-ethnic cohorts[23]. Additional variants in TM6SF2[24], MBOAT7[25], and HSD17B13[26] further define the genetic landscape, implicating lipid metabolism, inflammation, and fibrosis pathways. Despite these breakthroughs, the complexity of MASLD progression, shaped by genetic, metabolic, and environmental interactions, demands further research to elucidate stage-specific mechanisms and distinguish benign cases from progressive disease.

Histology has long been a cornerstone for understanding MASLD pathophysiology, but its limitations as a sole proxy for disease mechanisms are increasingly evident. Pseudo-temporal ordering, initially developed for microarray data[27] and now widely applied in single-cell genomics, provides an alternative framework by arranging cells or patients along trajectories based on their

85 molecular states. This approach has recently been used to study Alzheimer's disease progression
86 through brain expression data[28,29], and offers a promising, histology-independent method for
87 investigating MASLD progression via transcriptomic profiles. By complementing traditional
88 assessments, pseudo-temporal ordering provides a data-driven perspective on the molecular
89 changes underpinning disease progression.

90 In this study, we applied pseudo-temporal ordering to human MASLD/MASH liver transcriptomes
91 and integrated the resulting progression axis with co-expression and regulatory network analyses.
92 This framework resolved dynamic, stage-dependent transcriptional programmes across the
93 disease continuum and was reproducible across independent cohorts, including longitudinal
94 paired biopsies. By intersecting the disease network with liver–plasma-correlated proteins, we
95 further derived a 57-gene plasma-accessible biomarker panel that outperformed established non-
96 invasive scores for advanced fibrosis and enabled continuous patient positioning along the
97 molecular trajectory. Together, these results provide a scalable strategy for mapping MASLD
98 progression from cross-sectional data and for supporting non-invasive staging and longitudinal
99 monitoring.

100 Results

101 **Transcriptomics-based disease trajectory analysis captures MASLD**
102 **progression**.

103 We hypothesised that MASLD progression could be modelled as a continuum of patient states.
104 Given variability between patients, including the role of sex[30], comorbid conditions[31] and other
105 parameters in the timing of disease progression[32], we focused on modelling the molecular
106 underpinnings of the progression that are directly related to the histological phenotypes, as these
107 are common to all patients.

108 To test this hypothesis, we analysed RNA-seq data from 136 patients across two published
109 cohorts[14,33], adjusting for sex during data integration (Methods; **Supplementary Tables 1 & 2**).
110 After excluding one outlier, we applied pseudo-temporal ordering to derive a transcriptomics-
111 based disease trajectory (**Fig. 1A–B**; **Supplementary Fig. 1A-B**). The inferred trajectory showed
112 strong concordance with histological measures, including steatosis, ballooning, inflammation,
113 fibrosis, and NAS (Pearson R = 0.96–1.0; $p < 0.05$ for most compared disease stages; ANOVA

114 followed by Tukey's pairwise comparisons; **Supplementary Fig. 1C**), confirming alignment with
115 established disease stages.

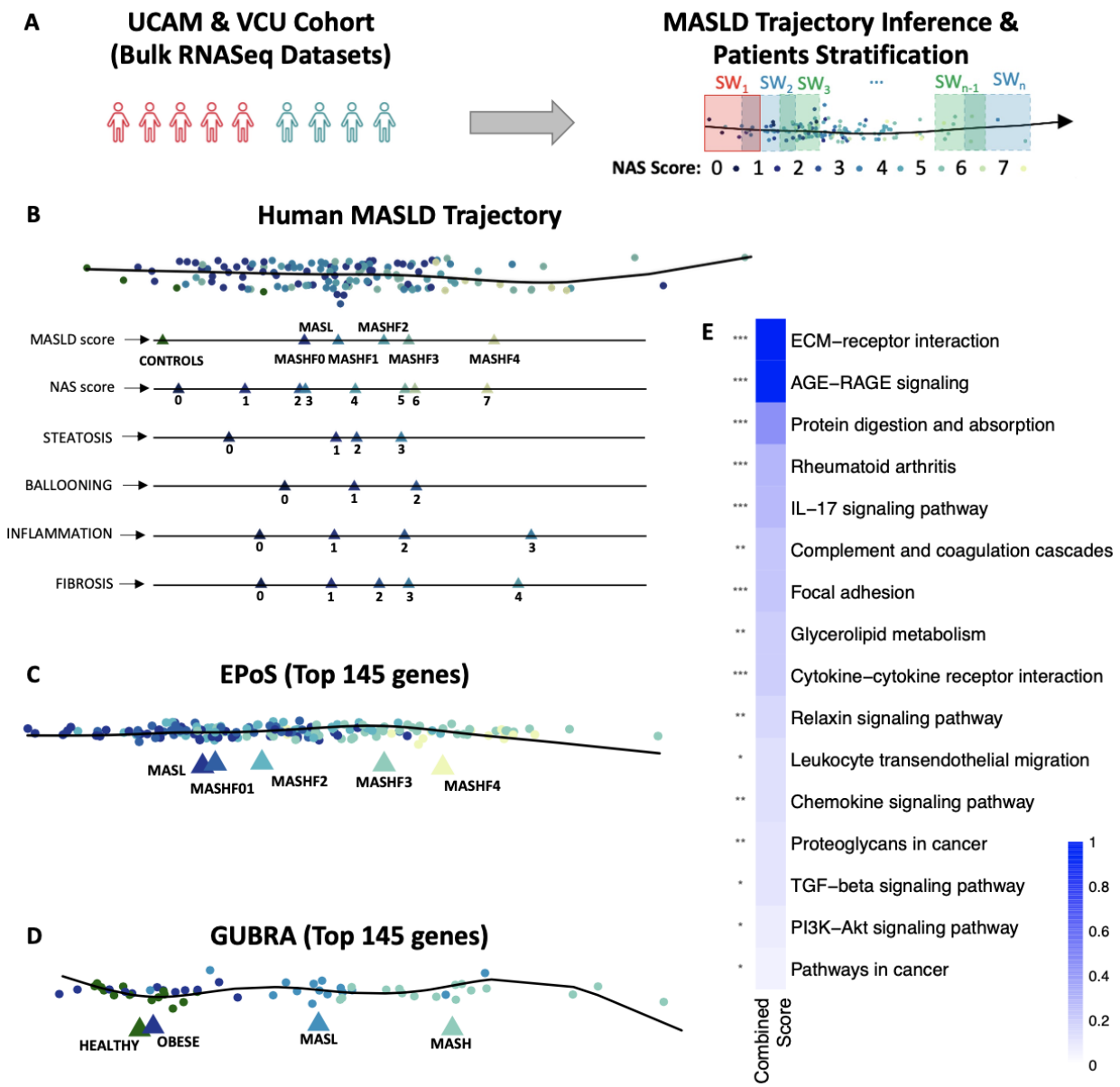

116
117 ***Figure 1. Pseudo-temporal ordering of patients captures disease progression and***
118 ***identifies MASLD gene signature. A.*** *Schematic of pseudotemporal ordering of patients based*
119 *on bulk transcriptomics data from liver biopsies and stratification of patients into sliding windows.*
120 ***B.*** *Pseudo-temporal ordering of patients based on transcriptomic data recapitulates disease*
121 *progression based on individual phenotypes, i.e., steatosis, ballooning, inflammation and fibrosis,*
122 *and based on the NAS and MASLD scores.* ***C-D.*** *Pseudotemporal ordering of two independent*
123 *orthogonal datasets, based on the 145 genes that are most predictive of the trajectory, provides*
124 *a linear and clear separation of the disease stages (EPoS dataset (**C**) and Gubra dataset (**D**)).*
125 *Triangles show the average position of each histopathologically characterised stage on the*

trajectory. ***E.*** *Functional enrichment analysis results of these 145 genes using EnrichR, where the Combined Score (c) has been calculated as c = log(p_value) * z_score, with p_value representing the Fisher exact test outcome, and z-score the deviation from the expected rank.*

To validate the trajectory model, we tested it on two independent RNA-Seq datasets: the EPoS dataset, a large multi-cohort dataset encompassing 168 MASLD patients across the full disease spectrum, and the Gubra dataset, comprising 26 healthy normal weight and obese individuals, and 31 MASLD and MASH patients[13,34]. Initial pseudotemporal ordering of these patients showed a trend of disease progression; however, additional variance in both datasets was observed that did not fully correlate with disease progression (**Supplementary Fig. 2A-B**).

To identify the principal drivers of variance along the MASLD/MASH trajectory and assess their generalisability, we applied a random forest approach to the discovery cohorts (UCAM/SANYAL), identifying 145 genes predictive of disease stage and histopathological features (AUC 0.62–0.73; **Supplementary Table 3**). This gene set more accurately recapitulated the disease trajectory in independent datasets[13,34], improving linearity and stage separation compared with the full transcriptome (**Fig. 1C–D**). Feature selection was performed exclusively on the discovery data, ensuring no information leakage and supporting the model's robustness across the larger, more heterogeneous EPoS and Gubra cohorts.

Finally, we evaluated the ability of our 145 gene signature to place longitudinal data from 58 patients from a different ethnic background (Japanese cohort[35]) along the trajectory. We found that their location on the trajectory was largely consistent with the changes in their histological profile, in particular where their disease regressed (**Supplementary Fig. 2C-E**). Together, these results demonstrate the generalisability of our 145 genes for MASLD trajectory inference.

The identified genes were enriched in pathways central to MASLD/MASH progression, including ECM-receptor interaction and focal adhesion (associated with fibrosis), AGE-RAGE and IL-17 signalling (inflammatory responses), and TGF-beta and PI3K-Akt signalling (wound healing and metabolic dysregulation). Other pathways, such as glycerolipid metabolism and cytokine-receptor interaction, reflect the metabolic and immune dysregulation characteristic of MASLD/MASH (**Fig. 1E**, **Supplementary Table 4**).

To enable deeper insights into the molecular changes driving MASLD progression, we next combined a sliding window (SW) approach, dividing patients into groups along the disease

157 trajectory, with network analysis. To optimise the sliding windows sequence, we developed a
158 graph-based method that maximised the information content of each window (Methods). Using
159 this approach, patients were divided into 13 subgroups along the trajectory for functional network
160 analysis (Methods; **Fig. 1A**; **Supplementary Fig. 3**; **Supplementary Tables 1 & 5**).

161 Data-Driven Global MASLD/MASH Network Recapitulates Key Molecular 162 Mechanisms of Disease

163 First, to construct a MASLD reference network, we adapted our previously published method for
164 generating phenotype-specific networks by integrating paired transcriptomics and phenotype
165 data[36] (**Fig. 2A**; Methods). Using Weighted Gene Co-expression Network Analysis (WGCNA)[37],
166 we identified gene co-expression modules and linked them to key phenotypic features, including
167 the NAS score, steatosis, ballooning, and fibrosis (**Fig. 2B**; **Supplementary Table 6**). The
168 ballooning score reflects hepatocyte injury, whereas the inflammation score, which reflects lobular
169 immune infiltrates. The inflammation score was used as a covariate in the analysis, due to
170 difficulty deconvolving its role as a cause vs. effect and because it dominated the signal.
171 Nonetheless it is already represented in the NAS score. Finally, to extract the modules associated
172 with our histological phenotypes of interest, we used linear regression, identifying 10 modules
173 associated with at least one phenotypic feature (**Fig. 2B**; Methods). After filtering genes that were
174 not correlated with the eigengene of each module (Methods), the number of genes in each
175 significant module ranged from 192 in the MEsalmon to 2949 in the MEturquoise module
176 (**Supplementary Table 6**).

177 Reactome[38] enrichment of the phenotype-associated modules highlighted patterns consistent
178 with MASLD progression (**Supplementary Table 7**). MEbrown, positively associated with
179 ballooning and fibrosis, showed exceptionally strong enrichment for protein translation (R-HSA-
180 72766, FDR = 1.9e-99) and ribosome biogenesis (R-HSA-72706, FDR = 5.5e-59), reflecting
181 hepatocyte stress and increased biosynthetic demand during injury[39]. MEred, also linked to
182 fibrosis and ballooning, was enriched for extracellular matrix organization (R-HSA-1474244, FDR
183 = 6.5e-23), aligning with well-established fibrogenic remodeling[40]. In contrast, MEblue, associated
184 with steatosis and NAS, was enriched for gene-regulatory programs (R-HSA-74160, FDR = 1.6e-
185 18) consistent with early metabolic and transcriptional reprogramming in lipid-laden
186 hepatocytes[41]. Finally, MEyellow, although negatively associated with fibrosis and ballooning,
187 showed strong enrichment for immune system pathways (R-HSA-168256, *FDR = 1.8e-47*),

188 capturing the inflammatory processes characteristic of advanced disease. Together, these
189 phenotype–pathway correspondences provide confidence that the reference network
190 recapitulates key molecular processes underlying steatosis, hepatocellular injury, inflammation,
191 and fibrosis in MASLD.

192 As a confirmation that our modules are indeed following the expected dynamics reflected in the
193 histology, we evaluated the 'activity' of the modules along our sliding window identifying two
194 groups (Methods): Modules that are generally associated with Fibrosis, Ballooning and NAS (e.g.
195 MEred, MEbrown and others; **Fig 2B-C**) being less active in the beginning of the trajectory and
196 peaking at the later stages, whereas those associated with Steatosis and NAS (e.g. MEblue,
197 MEturqoise) behaving oppositely. Interestingly, METan, which is mainly associated with
198 ballooning and NAS, only shows activity in the early-mid stages (SW5-7), in agreement with the
199 histology.

200 Transcription factor (TF) enrichment analysis of the phenotype-associated modules identified 199
201 TF regulons across nine out of the ten significant modules (FDR < 0.05), with many converging
202 on TGF-beta-driven fibrogenic signalling (**Supplementary Table 8**). Among these, 65 TFs were
203 shared across multiple modules (**Fig. 2D**). Core TGF-beta regulators SMAD2, 3 and 4, were
204 selectively enriched in the MEred module (FDR = 0.04, 5e-05, 6.3e-08 respectively;
205 **Supplementary Table 8**), consistent with its link to ballooning and fibrosis (**Fig. 2B**). Enriched in
206 the ballooning and fibrosis-associated modules, we found SP1, SRF, and ETS1, known to interact
207 with TGF-beta signalling to promote the expression of tissue remodelling and fibrosis factors[42–44].
208 EGR1, a TGF-beta–responsive TF previously linked to both steatosis and fibrosis[45,46,47], was
209 enriched across multiple modules, bridging early and late disease features (**Fig. 2D**).

210 HNF4A, a key regulator of liver development and morphogenesis[48], and PPARG, which controls
211 lipid storage and adipocyte differentiation in liver[49], appeared across modules with opposing
212 phenotype associations (MEbrown versus MEturquoise or MEyellow; FDR HNF4A = ~0.001,
213 PPARG = 1e-04 and 4.3e-05; **Fig. 2B & D**), indicating divergent transcriptional programmes
214 across disease stages. SREBF1, found in MEyellow (FDR = 0.05) and MEmagenta (FDR = 0.04),
215 similarly bridges lipogenic regulation and early stress responses, consistent with its shift from
216 metabolic control toward activation under hepatocellular injury[33,50].

217

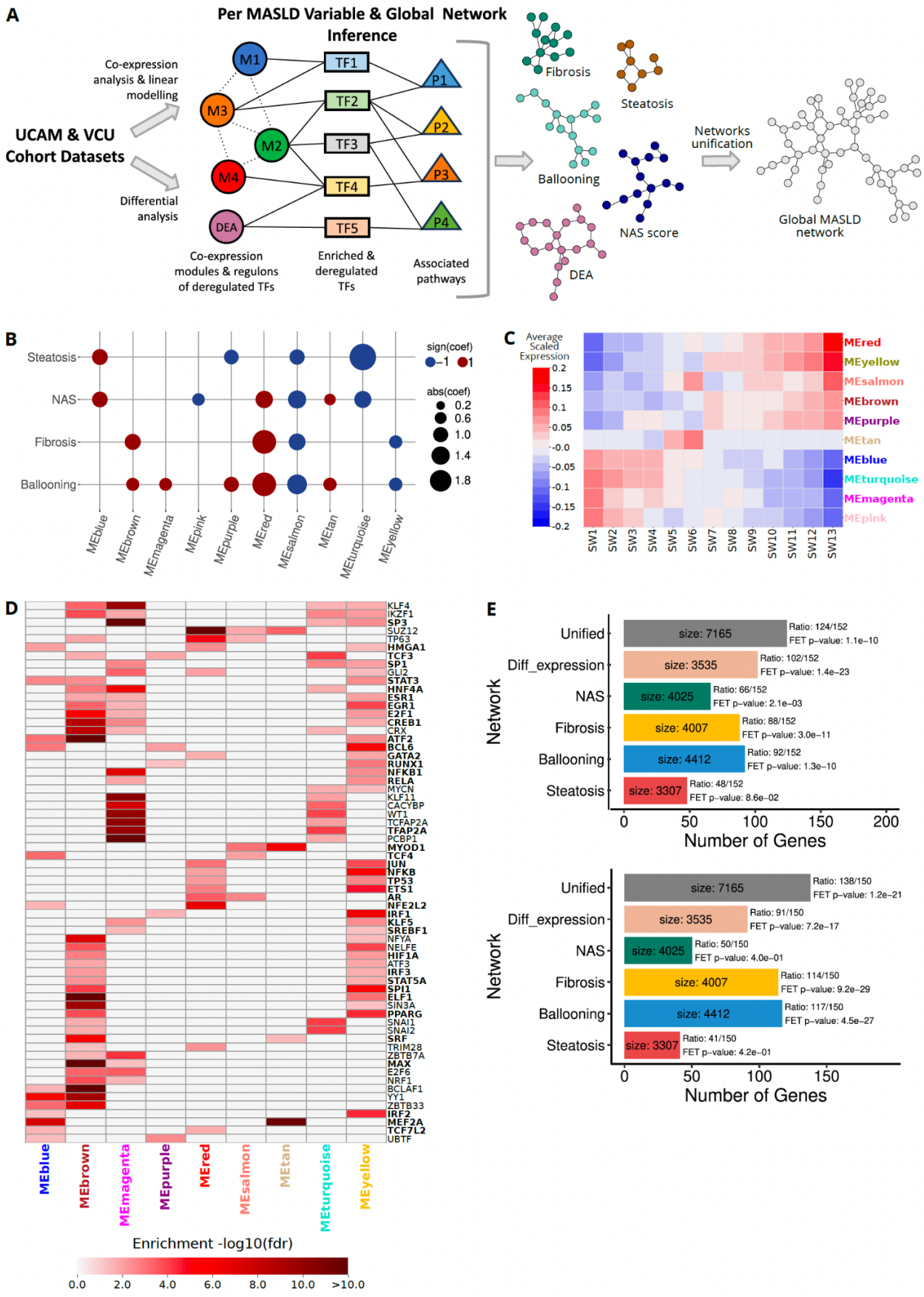
A
Per MASLD Variable & Global Network Inference
UCAM & VCU Cohort Datasets
Co-expression analysis & linear modelling
Differential analysis
M1
M2
M3
M4
DEA
TF1
TF2
TF3
TF4
TF5
P1
P2
P3
P4
Co-expression modules & regulons of deregulated TFs
Enriched & deregulated TFs
Associated pathways
Fibrosis
Steatosis
Ballooning
NAS score
DEA
Networks unification
Global MASLD network
B
Steatosis
NAS
Fibrosis
Ballooning
MEblue
MEbrown
MEmagenta
MEpink
MEpurple
MEred
MEsalmon
MEtan
MEturquoise
MEyellow
sign(coef)
-1
1
abs(coef)
0.2
0.6
1.0
1.4
1.8
C
Average Scaled Expression
0.2
0.15
0.1
0.05
0.0
-0.05
-0.1
-0.15
-0.2
MEred
MEyellow
MEsalmon
MEbrown
MEpurple
MEtan
MEblue
MEturquoise
MEmagenta
MEpink
SW1
SW2
SW3
SW4
SW5
SW6
SW7
SW8
SW9
SW10
SW11
SW12
SW13
D
KLF4
IKZF1
SP3
SUZ12
TP63
HMGA1
TCF3
SP1
GLI2
STAT3
HNF4A
ESR1
EGR1
E2F1
CREB1
CRX
ATF2
BCL6
GATA2
RUNX1
NFKB1
RELA
MYCN
KLF11
CACYBP
WT1
TCFAP2A
TFAP2A
PCBP1
MYOD1
TCF4
JUN
NFKB
TP53
ETS1
AR
NFE2L2
IRF1
KLF5
SREBF1
NFYA
NELFE
HIF1A
ATF3
IRF3
STAT5A
SPI1
ELF1
SIN3A
PPARG
SNAI1
SNAI2
SRF
TRIM28
ZBTB7A
MAX
E2F6
NRF1
BCLAF1
YY1
ZBTB33
IRF2
MEF2A
TCF7L2
UBTF
MEblue
MEbrown
MEmagenta
MEpurple
MEred
MEsalmon
MEtan
MEturquoise
MEyellow
Enrichment -log10(fdr)
0.0
2.0
4.0
6.0
8.0
10.0
>10.0
E
Network
Unified
Diff_expression
NAS
Fibrosis
Ballooning
Steatosis
size: 7165
Ratio: 124/152
FET p-value: 1.1e-10
size: 3535
Ratio: 102/152
FET p-value: 1.4e-23
size: 4025
Ratio: 66/152
FET p-value: 2.1e-03
size: 4007
Ratio: 88/152
FET p-value: 3.0e-11
size: 4412
Ratio: 92/152
FET p-value: 1.3e-10
size: 3307
Ratio: 48/152
FET p-value: 8.6e-02
0
50
100
150
200
Number of Genes
Network
Unified
Diff_expression
NAS
Fibrosis
Ballooning
Steatosis
size: 7165
Ratio: 138/150
FET p-value: 1.2e-21
size: 3535
Ratio: 91/150
FET p-value: 7.2e-17
size: 4025
Ratio: 50/150
FET p-value: 4.0e-01
size: 4007
Ratio: 114/150
FET p-value: 9.2e-29
size: 4412
Ratio: 117/150
FET p-value: 4.5e-27
size: 3307
Ratio: 41/150
FET p-value: 4.2e-01
0
50
100
150
Number of Genes

218

Figure 2. Phenotype-specific gene modules associated with the different MASLD variables. ***A.*** *Schematic of the approach to extract a reference MASLD network.* ***B.*** *Association (coefficient from linear model) of the different gene co-expression modules with NAS score, Steatosis, Ballooning, and Fibrosis. Red indicates a positive coefficient, whereas blue indicates negative coefficient.* ***C.*** *Heatmap is showing the average scaled expression of the modules along the pseudotemporal trajectory. The values for each module were calculated by averaging the scores of SW-grouped samples along its first principal component (eigengene).* ***D.*** *TFs whose regulons are enriched in the modules. The figure shows TFs per module, coloured according to the adjusted p-value of the enrichment test. The presented TFs have been identified as enriched in multiple modules. Bold indicates TFs significantly deregulated (FDR<0.05) in at least one sliding window (see sliding window analysis results). The complete list of TFs derived from the enrichment analysis is given in* ***Supplementary Table 8.*** ***E.*** *Enrichment of MASLD network and its components in known MASLD genes curated from the literature (top) or from MSigDB (bottom).*

Inflammatory and hypoxia-responsive TFs (NFKB1, RELA, HIF1A) were enriched in MEyellow (FDR = 6.8e-11, 9.6e-11, and 0.006 respectively), whereas CREB1 showed strongest enrichment in MEbrown (FDR = 2.0e-24), reflecting distinct immune-driven[51,52,53] versus hepatocyte-intrinsic[54] stress transcriptional contexts (**Fig. 2B & D; Supplementary Table 8**).

To ensure comprehensive regulatory coverage, we additionally incorporated TFs differentially regulated along the disease trajectory (FDR < 0.05; Methods), yielding a combined TF module (DEA), in which 85 of the 199 enriched TFs showed stage-specific deregulation. (**Supplementary Table 8**).

We then integrated the phenotype-associated modules, their enriched TFs, and corresponding pathways (**Supplementary Table 9**; Methods) to construct module-specific regulatory networks for each histological feature, as well as for our dynamically regulated TFs along the disease trajectory (**Fig. 2A**). These networks were then merged into a comprehensive MASLD/MASH disease network, henceforth referred to as the MASLD network for simplicity, to capture dynamic changes in cellular processes across disease stages (**Fig. 2A**; Methods; **Supplementary Table 10**). The resulting network contained 7,165 nodes and showed significant enrichment for previously reported MASLD-associated genes from both our curated literature set (**Supplementary Table 11**) and an established MSigDB[55] gene set (MSigDB ID: M39806; Methods) (**Fig. 2E**).

As an orthogonal validation we used the same pipeline to generate a MASLD network using the larger EPoS dataset described above[13,34]. That network comprised 6,732 nodes (**Supplementary**

253 **Table 10**) and the intersection of the two networks was 5,241 nodes (Jaccard index=0.61, odds
254 ratio=7.11, Fisher's exact test p-value=0).

255 Sliding Window Analysis Highlights Molecular Dysregulation in MASLD 256 Progression

257 We next sought to combine our reference MASLD network with our patient trajectory by using our
258 sliding window approach (**Fig 1A**) to explore the molecular mechanisms unerlying MASLD
259 progression relevant to observed histological phenotypes.

260 Initially, we identified TFs that were dynamically regulated across MASLD progression, showing
261 strong concordance with traditional stage-based stratifications (early, middle, late and NAS score-
262 based patient stratification), while providing greater temporal resolution (**Fig. 3A**; **Supplementary**
263 **Table 12**). In total, 122 TFs exhibited at least one significant deregulation event along the
264 trajectory (FDR < 0.05), of which 57 were also detected by early–middle–late or NAS-based
265 analyses with concordant directionality. This shared set included TF clusters enriched for Toll-like
266 receptor signalling (e.g. FOS, JUN, CREB1, TP53, NFKB1/2, RELA; R-HSA-168898, FDR = 5.3e-
267 05), estrogen receptor–mediated signalling (e.g. ESR1, RUNX1, MYB; R-HSA-8939211, FDR =
268 6.4e-07), and cytokine signalling (e.g. EGR1, IRF and STAT family members; R-HSA-1280215,
269 FDR = 2.8e-08) (**Supplementary Figure 4**).

270 SREBF1 was consistently upregulated in early and intermediate disease states across all
271 stratifications (in SW4 and SW9 according to the SW approach), confirming its pro-steatotic
272 role[33,56], but only the trajectory-based and NAS-based approaches captured its downregulation in
273 later stages[57], illustrating the benefit of increased granularity.

274 Beyond this shared signal, the trajectory-based approach uniquely identified several key
275 regulatory events missed by discrete classifications, including early downregulation of HNF4A
276 (SW5), NR1I3 (SW5), and HNF1A (SW3 & 5), reflecting disrupted hepatocyte metabolic identity,
277 inflammatory signalling, and tissue remodelling[58,59,60] (**Fig. 3A**). Conversely, sustained
278 upregulation of pro-fibrotic regulators such as SRF[43] and dynamic regulation of TGF-β pathway
279 components, including downregulation of the inhibitory SMAD7[61] (SW2), were detected only along
280 the SW trajectory (**Fig. 3A**). Additional TFs (e.g. MYC, STAT1, NFKB1) displayed complex, stage-
281 dependent regulation, underscoring the ability of trajectory-based analysis to capture nuanced
282 and biologically meaningful regulatory dynamics during MASLD progression (**Fig. 3A**).

283 These results were largely validated in an orthogonal analysis of the EPoS dataset[13,34], where 69
284 TFs were deregulated in at least one SW, 57 of which overlapped with our primary analysis
285 (Jaccard index = 0.43, odds ratio = 76.03, Fisher's exact test p-value < 2.2e-16). Deregulation
286 directionality, based on cumulative activation scores, showed high concordance between
287 datasets with an average Pearson correlation coefficient (PCC) of 0.56 (**Supplementary figure**
288 **5A**). The average PCC of cumulative activities per SW was 0.38, revealing two opposing trends
289 along the disease trajectory (**Supplementary figure 5B**). Notably, PCC decreased monotonically
290 in early stages (SW2–SW5), indicating divergence in early molecular profiles between cohorts,
291 likely due to the absence of healthy samples and higher MASLD variable values in SW1 of the
292 EPoS dataset,which makes this group more similar to SW2 than in the UCAM/VCU cohort. In
293 contrast, PCC increased in middle and late stages, demonstrating that despite cohort-specific
294 differences, the trajectory-based approach captures consistent molecular programmes as
295 disease progresses (**Supplementary figure 5B**).

296 An intriguing cluster of TFs, including MEF2A, MEF2C, MEF2D, MYOG, NKX2-5, and ZBTB4,
297 exhibited unique activity patterns in our trajectory analysis that were not detected using traditional
298 discrete patient staging (**Fig. 3A**). Their activity peaked during SW5–SW6 and then sharply
299 declined at SW7, suggesting either a resolution of activation or a shift in regulatory dynamics.
300 Notably, no significant changes in their activity were observed in later stages, indicating a potential
301 stabilisation of their regulatory influence as the disease progressed (**Fig 3A**). These TFs, known
302 primarily for their roles in myogenesis[62], have also been implicated in hepatic stellate cell
303 activation and their transition to a myofibroblast-like phenotype, a critical driver of fibrosis[63].
304 MEF2A/MEF2C and NKX2-5 also have documented roles in macrophage differentiation and
305 inflammatory programming[64–66], although not specifically related to MASLD. Further research is
306 needed to understand the role of this TF cluster in MASLD progression.

307 To explore the underlying molecular processes, we employed a network propagation-based
308 strategy to extract differentiated network signatures for each sliding window from the MASLD
309 reference network (Methods). Reactome analysis of these networks identified 111 pathways
310 exhibiting progressive changes along the disease trajectory (**Supplementary Fig. 6**;
311 **Supplementary Table 13; Methods**). Signal transduction, including TGF beta, Receptor
312 Tyrosine Kinase and others, and multiple immune pathways increased with disease progression
313 (**Supplementary Fig. 6**), consistent with escalating inflammatory and signalling dysregulation.
314 Extracellular matrix organisation pathways, linked to fibrosis, such as integrin and non-integrin

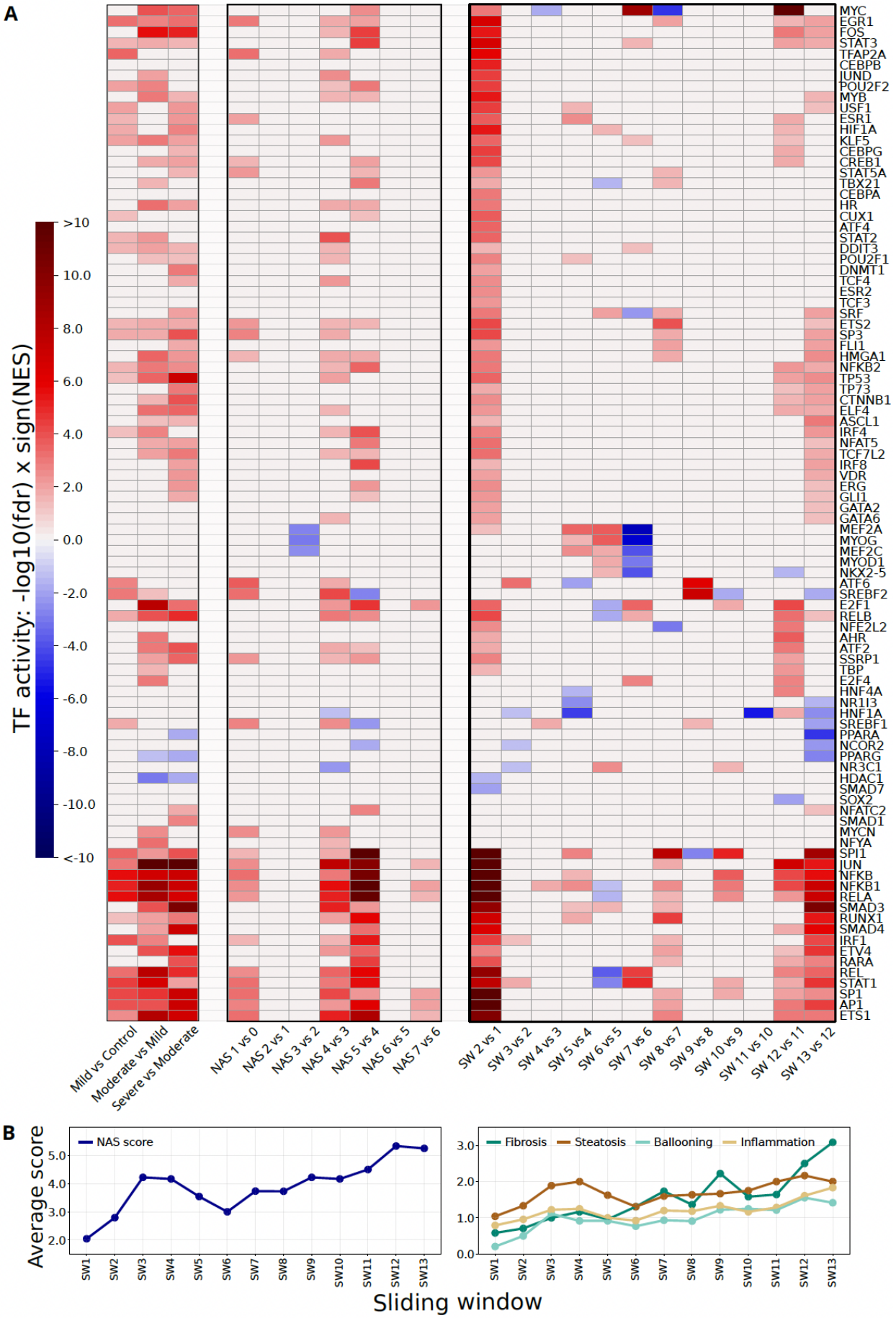
A
TF activity: -log10(fdr) x sign(NES)
>10
10.0
8.0
6.0
4.0
2.0
0.0
-2.0
-4.0
-6.0
-8.0
-10.0
<-10
MYC
EGR1
FOS
STAT3
TFAP2A
CEBPB
JUND
POU2F2
MYB
USF1
ESR1
HIF1A
KLF5
CEBPG
CREB1
STAT5A
TBX21
CEBPA
HR
CUX1
ATF4
STAT2
DDIT3
POU2F1
DNMT1
TCF4
ESR2
TCF3
SRF
ETS2
SP3
FL1
HMGA1
NFKB2
TP53
TP73
CTNNB1
ELF4
ASCL1
IRF4
NFAT5
TCF7L2
IRF8
VDR
ERG
GLI1
GATA2
GATA6
MEF2A
MYOG
MEF2C
MYOD1
NKX2-5
ATF6
SREBF2
E2F1
RELB
NFE2L2
AHR
ATF2
SSRP1
TBP
E2F4
HNF4A
NR1I3
HNF1A
SREBF1
PPARA
NCOR2
PPARG
NR3C1
HDAC1
SMAD7
SOX2
NFATC2
SMAD1
MYCN
NFYA
SPI1
JUN
NFKB
NFKB1
RELA
SMAD3
RUNX1
SMAD4
IRF1
ETV4
RARA
REL
STAT1
SP1
AP1
ETS1
Mild vs Control
Moderate vs Mild
Severe vs Moderate
NAS 1 vs 0
NAS 2 vs 1
NAS 3 vs 2
NAS 4 vs 3
NAS 5 vs 4
NAS 6 vs 5
NAS 7 vs 6
SW 2 vs 1
SW 3 vs 2
SW 4 vs 3
SW 5 vs 4
SW 6 vs 5
SW 7 vs 6
SW 8 vs 7
SW 9 vs 8
SW 10 vs 9
SW 11 vs 10
SW 12 vs 11
SW 13 vs 12
B
Average score
NAS score
5.0
4.0
3.0
2.0
SW1
SW2
SW3
SW4
SW5
SW6
SW7
SW8
SW9
SW10
SW11
SW12
SW13
Fibrosis
Steatosis
Ballooning
Inflammation
3.0
2.0
1.0
0.0
Sliding window

316 ***Figure 3. Sliding window analysis to study the landscape of molecular changes along the***
317 ***MASLD trajectory. A.*** *Results from TF activity analysis in two types of discrete patient*
318 *stratification (Mild, Moderate, Severe and NAS scores), and the pseudotemporal trajectory. The*
319 *colour indicates a change in TF activity compared to the previous disease stage.* ***B.*** *Mean*
320 *phenotype and NAS pathologist scores along the SW trajectory.*

321

322 membrane-ECM interactions, were upregulated predominantly from mid to late stages
323 (**Supplementary Fig. 6**). Metabolic pathways showed more complex dynamics: lipid metabolism
324 was initially downregulated (SW3-5) but showed modest upregulation after SW8, whereas
325 glucose metabolism increased persistently from early stages, consistent with insulin resistance[67].
326 Orthogonal validation in the EPoS dataset[13,34] identified 95 associated pathways, with 72
327 overlapping (Jaccard index = 0.54, odds ratio = 7.23, Fisher's exact test p-value = 6.3e-12;
328 **Supplementary Table 13**). Pathway deregulation directionality was concordant across datasets
329 (average PCC = 0.46; **Supplementary Fig. 7A**), and cumulative pathway activities per SW
330 showed even higher agreement (average PCC = 0.52; **Supplementary Fig. 7B**), mirroring
331 oscillatory patterns observed in TF-based analyses but with higher overall correlation.

332 Finally, we compared pathway dysregulation across sliding windows with histopathological scores
333 (steatosis, ballooning, inflammation, fibrosis, and NAS; **Fig. 3B**). Although these scores increased
334 overall with disease progression, several pathways showed dysregulation earlier than histological
335 changes. For example, extracellular matrix pathways were upregulated at SW8, receding the
336 overall increase in fibrosis observed later along the trajectory., aligned with significant changes in
337 multiple TFs (**Fig. 3A**) in that stage, indicating that molecular readouts may detect MASLD
338 progression earlier than conventional assessments.

339 Overall, the enhanced resolution of our sliding window-based approach provides a
340 comprehensive molecular landscape of MASLD progression, shedding light on the interplay
341 between immune activation, fibrotic remodelling, and metabolic dysregulation over time.

342 Cell-Type Deconvolution Along the MASLD Trajectory Reveals Network
343 Changes Associated with Tissue Composition

344 Changes in liver cell composition and state are hallmarks of MASLD progression and reflect
345 injury- and inflammation-driven remodelling of the hepatic microenvironment[1]. Characterising the

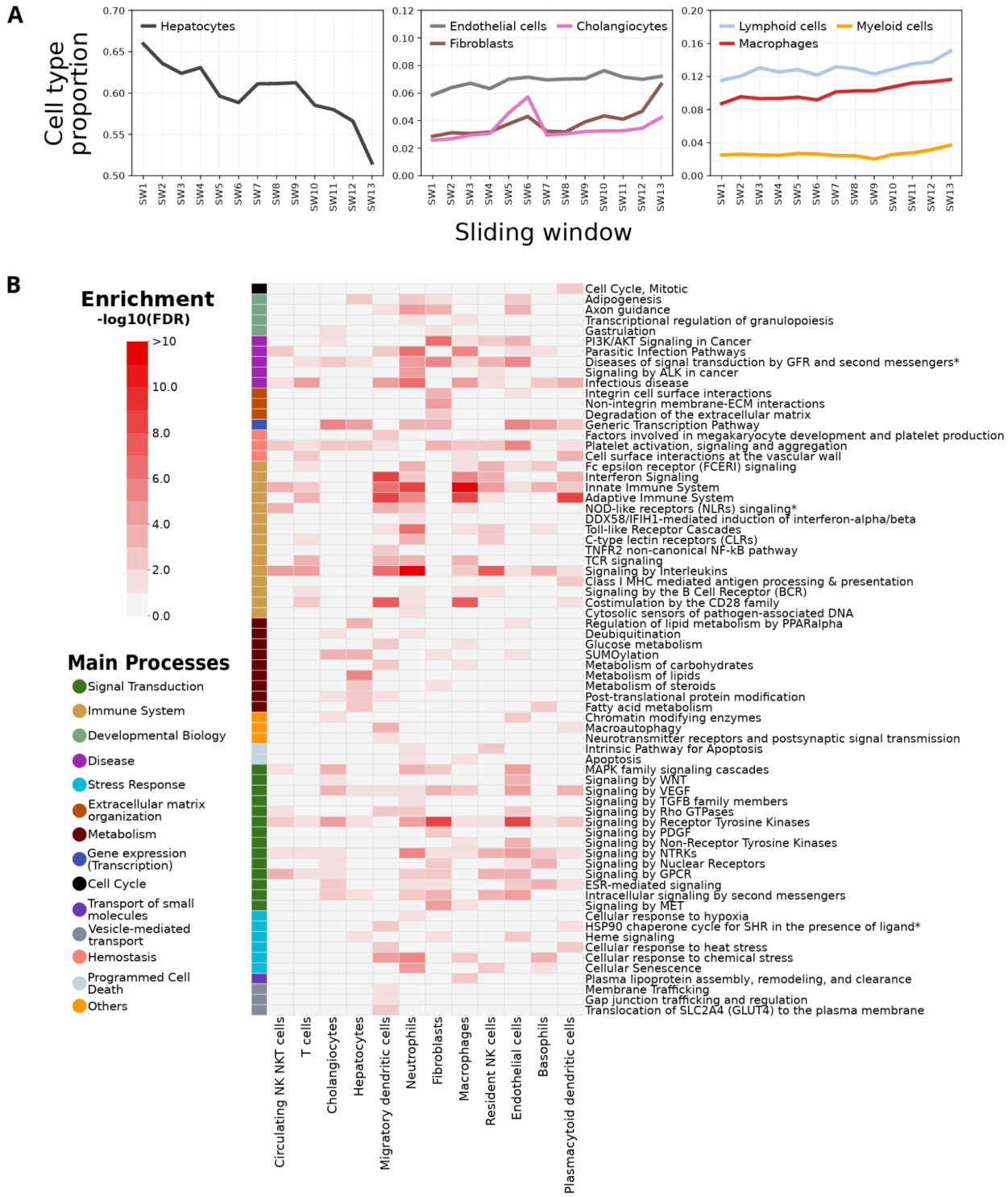

Figure 4. Results of cell type deconvolution analysis. A. *Cell type deconvolution of patient transcriptomic data along our MASLD trajectory* ***B.*** *Prediction of cell types with which the deregulated processes are associated after excluding gene sets of these processes that could have been identified as differentiated by the mere change in abundance of cell types.*

351 molecular programmes underlying these shifts can help contextualise disease mechanisms and
352 inform biomarker discovery.

353 To characterise cellular dynamics along the trajectory, we performed cell-type deconvolution of
354 bulk liver transcriptomes (Methods; **Supplementary Fig. 8**; **Supplementary Table 14**).
355 Hepatocytes remained the dominant cell type but progressively declined from early to late stages
356 (from 0.66 in SW1 to 0.52 in SW13), consistent with increasing contributions from other hepatic
357 and immune populations. To obtain robust estimates, hematopoietic cells were aggregated into
358 myeloid and lymphoid lineages, excluding macrophages, which showed a distinct and progressive
359 increase, particularly after mid-progression (SW6; **Fig. 4A; Supplementary Fig. 8**). Lymphoid
360 cells (predominantly T cells and NK/NKT cells) increased more markedly than other myeloid
361 populations, alongside rising cholangiocyte and fibroblast signals, reflecting heightened
362 inflammatory and fibrogenic activity. In this analysis, the "fibroblast" annotation predominantly
363 reflects hepatic stellate cells, which comprise ~70% of this category in the reference single-cell
364 atlas[68]. In contrast, endothelial cell proportions remained relatively stable, suggesting
365 preservation of vascular structure even in advanced disease.

366 We next linked cell types to deregulated processes along the trajectory. To distinguish true
367 process dysregulation from shifts in cell composition, we removed genes whose expression
368 changes could be explained by changing cell proportions, using pseudo-bulk profiles derived from
369 healthy liver single-cell data (Methods).

370 Enrichment analysis of the remaining gene sets revealed cell type–specific pathway associations
371 (**Fig. 4B**; **Supplementary Table 15**). As expected, lipid metabolism was primarily hepatocyte-
372 associated, immune pathways mapped mainly to macrophages, neutrophils, and migratory
373 dendritic cells, and extracellular matrix and fibrotic processes were strongly linked to fibroblasts
374 (**Fig. 4B**). Non-immune signalling pathways, including Wnt, receptor tyrosine kinase, and Rho
375 signalling, were predominantly associated with endothelial cells, with additional contributions from
376 fibroblasts, cholangiocytes, and immune cells. Together, these results highlight coordinated
377 crosstalk between parenchymal, stromal, and immune compartments during MASLD progression.

378

MASLD Trajectory-Specific Biomarkers Through Integrated Plasma-Liver Expression Analysis

To address the critical need for non-invasive diagnostic methods for MASLD/MASH staging, we sought to identify blood-based proteomics markers that predict a patient's MASLD stage. Govaere et al.[69] recently identified 194 genes with correlated expression in both blood plasma and liver across MASLD progression stages. We hypothesized that the 57 genes among these that were also present in our MASLD network are more likely to be directly involved in disease progression and are, thus, better suited for disease monitoring (**Fig. 5A; Supplementary Table 1**).

We trained a Random Forest classifier using the 57-gene set to predict fibrosis stage (F0–F2 vs F3–F4), achieving 86.2% accuracy in the UCAM/VCU cohort (AUC = 0.769). Applying the elbow method to feature importance yielded an optimal 15-gene subset, which might be more tractable for clinical application (**Fig. 5A; Supplementary Table 1**). Validation in two independent cohorts showed robust performance. Specifically, in the Fujiwara cohort[35], the model achieved an AUC of 0.803 (0.794 for 15 genes), outperforming established clinical scores (FIB-4, APRI, NFS; **Fig. 5B**), while in the EPoS cohort[13] it reached an AUC of 0.86 (0.85 for 15 genes), exceeding FIB-4 by 10% (**Fig. 5C**). In general our model outperformed FIB-4 in all evaluation metrics tested (**Fig. 5D**). Robustness analysis against 300 random 57-gene signatures confirmed superior performance of the curated gene set in both external datasets ($p < 1e-64$; **Supplementary Fig. 9A**).

We further tested model generalisability by applying the transcriptomics-trained classifier to plasma proteomic data, where it retained strong performance (AUC = 0.83; 0.785 for the 15-gene subset; **Fig. 5E**, **Supplementary Fig. 9B**; Methods). Together, these results demonstrate that the plasma-based gene signature generalises across cohorts, outperforms established non-invasive tests, and directly translates into blood proteomics.

To enable continuous patient positioning along the disease trajectory, we trained a random forest regression model using the 57-gene signature. In the UCAM/VCU cohort, the model achieved strong and consistent predictive performance (R^2 = 87.9%, p = 1.66e-08; MSE = 0.008 across 1000 iterations of 5-fold cross-validation), accurately recapitulating increasing MASLD severity (**Supplementary Fig. 9C–D**). Validation in the independent EPoS cohort[13] confirmed this performance (R^2 = 85.1%, p = 8.04e-62), with predicted positions tracking progressive MASLD

409 stages (**Supplementary Fig. 9E**), whereas random 57-gene signatures did not (R^2 = 0.14;
410 **Supplementary Fig. 9F**).

411 Further validation in the Gubra dataset[34] (Methods) demonstrated similar accuracy (R^2 = 85.6%,
412 p = 1.4e-26), correctly separating healthy/obese individuals from MASLD/MASH patients along
413 the trajectory (**Fig. 5F**, **Supplementary Fig. 9G**), with 89.2% of early-trajectory individuals
414 classified as healthy/obese and 89.7% of late-trajectory individuals as MASLD/MASH. Finally,
415 applying the same model to plasma proteomics data successfully recapitulated disease
416 progression at the protein level (p = 1.09e-18; **Fig. 5G–H**). Together, these results demonstrate
417 that the 57-gene signature robustly predicts MASLD progression across cohorts and omics layers,
418 supporting its potential for non-invasive staging and longitudinal monitoring.

419 To assess genetic support for the 57-gene MASLD biomarker panel, we queried the GWAS
420 Catalog (v1.0)[70]. Forty-seven of the 57 genes were associated with at least one complex trait,
421 predominantly related to metabolic, cardiovascular, and liver phenotypes (**Supplementary Fig.
422 10A–B; Supplementary Table 16**). Nearly half of the genes (27/57; 47.4%) were linked to
423 multiple trait categories, suggesting pleiotropy. Enrichment analysis confirmed significant
424 overrepresentation of metabolic (FDR = 2.33e-05), cardiovascular (FDR = 0.0021), and liver-
425 related traits (FDR = 0.0032) relative to background (**Fig. 5I**), providing genetic support for the
426 biological relevance of the biomarker panel.

427 To explore potential therapeutic intersections, we mapped approved and investigational
428 compounds to the 57-gene biomarker panel (**Supplementary Table 17**). This revealed drug–
429 target associations spanning core MASLD processes. For example small molecules targeting
430 COL3A1 had indications related to extracellular matrix remodelling and fibrotic disorders (e.g.
431 Dupuytren contracture, Peyronie disease), those targeting CXCL9 and SERPINE1 are indicated
432 for inflammatory and immune signalling-related conditions (e.g. chronic bronchitis or Alzheimer's
433 disease as well as various cancers). Small molecules with indications for coagulation and vascular
434 diseases, such as atrial fibrillation, acute coronary syndrome or chronic kidney disease, target
435 F11 and AGT, and metabolic or hepatocellular stress pathway-related indications were linked to
436 ACAT2 and GPC3. Although exploratory, these patterns reinforce the biological relevance of the
437 biomarker panel and illustrate how a trajectory- and network-informed framework can support
438 hypothesis generation for biomarker-guided, stage-aware therapeutic prioritisation in MASLD.
439 Together, these results define a network-anchored and genetically supported biomarker

framework that captures MASLD progression as a continuous molecular trajectory and enables robust, non-invasive stratification of disease stage across cohorts and molecular layers.

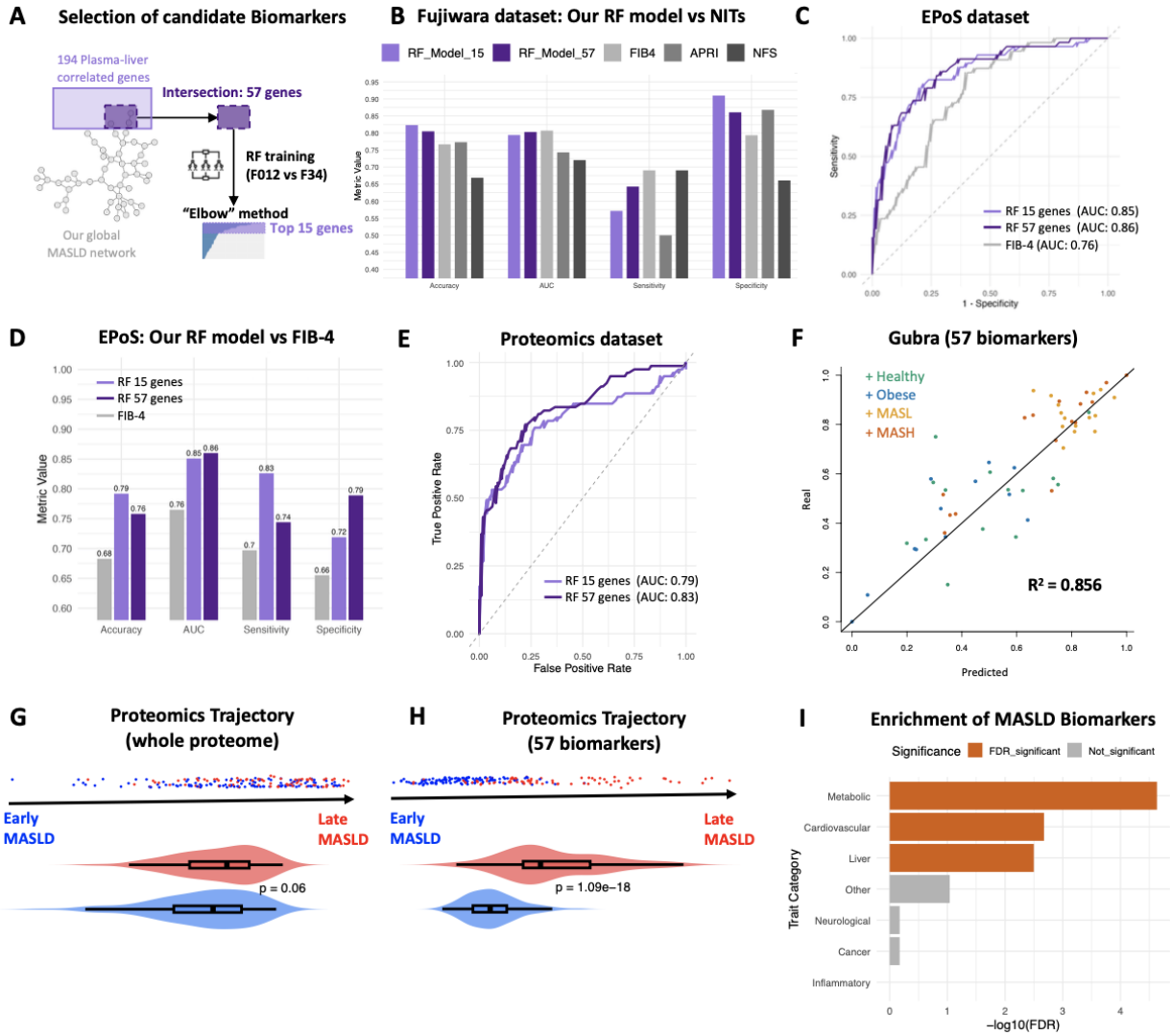

Figure 5. Biomarker selection and performance on the external liver transcriptomics and plasma proteomics datasets. A. *Selection of candidate biomarkers. A 57-gene set was defined by intersecting the global MASLD network with plasma–liver correlated genes[69], followed by random forest classification of fibrosis stage (F0–2 vs F3–4). Feature importance and the elbow method identified a reduced 15-gene subset.* ***B.*** *Performance of the 57- and 15-gene classifiers compared with non-invasive clinical scores in the Fujiwara cohort.* ***C-D.*** *Benchmarking of the same models against FIB-4 in the EPoS cohort, with C showing the ROC curve for our model compared to the FIB-4 score, and D showing the performance using additional metrics.* ***E.*** *ROC curve for fibrosis classification of patients using external plasma proteomics data.* ***F.*** *Random forest regression predicting patient positions along the MASLD trajectory in the Gubra cohort; predicted positions (57 genes) versus transcriptome-derived positions are shown (R^2, Pearson correlation).* ***G-H.*** *Inferred patient trajectory positions on the external validation plasma proteomics dataset, using either the whole proteome (G) or only the 57 biomarkers (H).* ***I.*** *GWAS*

trait enrichment of the 57-gene biomarker panel; significant categories after FDR correction are shown in orange (Fisher's exact test on the biomarkers associated with each of those categories, against the whole GWAS as the background).

Discussion

MASLD has become a leading cause of chronic liver disease and liver transplantation worldwide[71], yet its clinical assessment and mechanistic interpretation still rely primarily on static, histology-defined stages. These categories only partially capture the continuous and heterogeneous nature of disease progression and provide limited insight into the regulatory processes that govern transitions between states. Here, we present a data-driven framework that reconstructs a population-level molecular continuum of MASLD progression from cross-sectional liver transcriptomes. This trajectory is not a simulation or patient-level predictor, but a statistical representation of shared molecular states aligned with histological phenotypes across cohorts, offering a scalable alternative for studying disease progression when longitudinal biopsy data are limited or unattainable.

The inferred trajectory showed strong concordance with steatosis, ballooning, inflammation, fibrosis, and NAS and identified a robust 145-gene signature predictive of histological scores that was reproducible across multiple independent datasets, including a large multi-centre cohort and a longitudinal dataset with paired biopsies. Although MASLD progression is not strictly unidirectional at the individual level, the reproducibility of this axis across cohorts supports the existence of a dominant molecular progression pattern shared across patients. By design, our framework emphasises common disease mechanisms rather than subgroup-specific modifiers, such as sex, diabetes status, or BMI, which were corrected for during integration or did not dominate trajectory placement in this setting. This focus highlights convergent regulatory programmes that may be broadly targetable across patient populations, while providing a foundation for future stratified analyses as larger, metadata-rich cohorts become available.

Integrating co-expression analysis with transcription factor (TF) enrichment and upstream pathway information yielded a MASLD regulatory network enriched for established disease genes and validated in an independent large cohort. While module–phenotype associations remain correlative, anchoring the network to TFs and signalling pathways improves interpretability of upstream regulatory processes, as we have previously demonstrated[36]. TF-based pathway analysis refined established MASLD biology by showing that ER stress (R-HSA-380994) and

488 KEAP1–NFE2L2 oxidative-stress signalling (R-HSA-3299685) were selectively enriched in
489 ballooning- and fibrosis-associated TF sets, rather than in steatosis-associated TF sets,
490 suggesting that these stress-response programmes emerge primarily during hepatocyte injury. In
491 addition, fibrosis-specific enrichment of TP53 regulatory signalling (R-HSA-3700989) and
492 adherens junction interactions (R-HSA-373760) highlights transcriptional and structural
493 remodelling processes that are less emphasised in conventional MASLD pathway analyses.

494 By resolving progression into overlapping sliding windows rather than discrete stages, the
495 framework captured dynamic regulatory behaviours that traditional staging obscures. Immune-
496 related TFs and pathways, including NF-κB and STAT signalling, were sustained across the
497 trajectory, consistent with chronic inflammatory signalling in MASLD. In contrast, profibrotic and
498 myogenic TFs, including MEF2 family members, exhibited a transient peak during mid-
499 progression.

500 Pathway-level analysis further revealed temporally ordered activation of hypoxia responses,
501 extracellular matrix remodelling, and growth factor signalling (e.g., WNT[72], PDGF[73], TGF-β[74]),
502 alongside non-monotonic metabolic changes. Persistent upregulation of glucose metabolism
503 across the trajectory is consistent with hepatic and systemic insulin resistance. In contrast, lipid
504 metabolism showed early suppression followed by partial reactivation, underscoring the
505 complexity of metabolic dysfunction during disease progression.

506 MASLD progression is accompanied by shifts in liver cell composition driven by cellular plasticity,
507 including stellate cell activation and hepatocyte–cholangiocyte transdifferentiation[75]. Cell-type
508 deconvolution showed reduced hepatocyte signal and increased contributions from immune,
509 cholangiocyte, and fibroblast cell types, consistent with known histological changes. Macrophage
510 signals increased along the trajectory and aligned with inflammatory pathways, supporting their
511 established role in steatohepatitis[59,76]. Fibroblast-associated signatures, largely reflecting hepatic
512 stellate cells within the reference atlas, were linked to extracellular matrix remodelling, whereas
513 metabolic dysregulation was predominantly hepatocyte-driven. Although bulk deconvolution
514 primarily supports relative trends rather than precise cell proportions, these findings are consistent
515 with current models of MASLD and motivate future validation using single-cell[75] and spatial[77]
516 approaches.

517 A key contribution of this study is the derivation of a 57-gene plasma-accessible biomarker panel,
518 anchored in the MASLD regulatory network and validated across independent cohorts and omics

519 layers. Unlike biomarker approaches based solely on predictive feature selection, this panel
520 prioritises mechanistic relevance by linking circulating markers to disease-associated regulatory
521 programmes and genetic evidence. The biomarker panel outperformed established non-invasive
522 scores, including FIB-4, APRI, and NFS, in distinguishing advanced fibrosis and enabled
523 continuous placement of patients along the molecular trajectory. Furthermore, it aligns with
524 established fibrosis-associated signatures, overlapping with clinically validated markers such
525 as A2M (component of the NIS4 fibrosis test[78]), FAP (associated with PRO-C3 related
526 fibrogenesis[79,80]) and THBS2[81,82]. Importantly, our biomarker panel resolves into mechanistic
527 axes central to MASLD progression, including extracellular matrix remodelling, immune
528 activation, metabolic stress, and coagulation–vascular pathways[83].

529 Although these biomarkers are not yet ready for clinical application, their consistent performance
530 across transcriptomic and proteomic datasets and their relevance to known processes related to
531 MASLD progression, supports the value of network-informed biomarker discovery in MASLD and
532 motivates prospective validation. In this context, the observation that these biomarkers intersect
533 with known pharmacological targets across fibrotic, inflammatory, vascular, and metabolic
534 pathways further highlights the potential of a trajectory-informed framework to support stage-
535 aware therapeutic hypothesis generation.

536 This study has limitations. The trajectory captures shared molecular progression but cannot infer
537 causality or predict individual disease courses. Cross-sectional data limit inference on reversibility
538 and treatment effects, and subgroup-specific modifiers such as sex, diabetes, and medication use
539 are not explicitly modelled. Nonetheless, the resulting MASLD network provides a structured
540 framework for contextualising molecular dysregulation, identifying stage-associated regulatory
541 programmes, and prioritising candidate pathways for further investigation. Incorporation of
542 longitudinal sampling, richer clinical metadata, and single-cell or spatial data will be important next
543 steps to refine this framework and extend it toward stratified and personalised analyses.

544 In summary, this work provides a unified, trajectory-based molecular framework for MASLD that
545 organises established disease mechanisms into a coherent and reproducible progression model.
546 By integrating regulatory networks, pathway dynamics, and non-invasive biomarkers, the
547 framework advances beyond static staging. It, thus, offers a scalable approach for studying
548 MASLD and other progressive diseases or biological trajectories characterised by cross-sectional
549 molecular data.

Materials & Methods

Datasets

For the analyses conducted in this study, 2 different publicly available human datasets have been used: the "UCAM" dataset[33] (consisting of 58 consecutive patients recruited at the MASH Service at the Cambridge University Hospital) and the VCU dataset[14] (consisting of 4 obese bariatric controls without MASLD and 74 patients covering the whole MASLD spectrum). The raw transcriptomic data and relevant metadata have been downloaded from Array Express (E-MTAB-9815) and NCBI's GEO (GSE130970), respectively. Details for both datasets are given in **Supplementary Tables 1 & 2**. “Sample_5” was removed from the analysis as it was considered an outlier (Supplementary Fig. 11A-B).

For the validation of the human trajectory inference method, we used three publicly available transcriptomics datasets (GUBRA[34,84] , EPoS[13], Fujiwara[35]) and the Govaere proteomics dataset[69] was used for the biomarker analysis. The GUBRA dataset consists of n=26 healthy (n=14 normal-weight, n=12 overweight) individuals recruited at the Center for Diabetes Research (Copenhagen University, Denmark) and n=31 MASLD/MASH patients recruited at the Department of Hepatology and Gastroenterology (Aarhus University Hospital, Denmark). The EPoS dataset consists of 168 MASLD/MASH patients, originates from a large cohort recruited in multiple European parts, and has been previously used by our team[85]. In addition to the expression data, the EPoS dataset also provided information on the MASLD disease stage, NAS, Fibrosis stage, and Fibrosis-4 (FIB-4) scores per patient. The Fujiwara[35] dataset contains longitudinal transcriptomic data and metadata from 58 MASLD patients across two liver biopsies spanning the full disease spectrum. As non-invasive test (NIT) scores were not directly provided in the original published dataset, the FIB-4[5], AST-to-Platelet Ratio Index[86] (APRI), and NAFLD Fibrosis Score[4] (NFS) were calculated from the available metadata using standard, previously published definitions. Only samples with complete data required for each score were included in the corresponding analyses (**Supplementary Table 18**). Finally, the Govaere proteomics dataset[69] consists of paired plasma proteomics and liver transcriptomics data from 191 patients, including samples matched to the EPoS patients, enabling cross-omics validation of the trajectory model and biomarker analysis.

RNA-Seq Analysis and data processing

For the RNA-Seq analysis, the *FASTQC* software was used to generate quality-control (QC) reports of individual FASTQ files (http://www.bioinformatics.babraham.ac.uk/projects/fastqc, v. 0.11.9) and reads were aligned to the human GRCh38 reference genome using hisat2[87] (v 2.1.0). Then, the genes were counted with *HTSeq*[88] (v 0.11.1), and the *biomaRt package*[89] was used to map “Ensembl gene IDs” to “HGNC symbols”.

We used quantile normalisation to normalise the 2 datasets and Bioconductor's function *COMBAT*[90] from R package *sva* to remove the batch effect observed upon integrating them (**Supplementary Fig. 11A-B**). Sex was used as a covariate. Quality control checks validate the robustness of the analysis, showing that the gene expression in each MASLD stage, separately for each dataset, remains similar after batch effect correction (**Supplementary Fig. 11C-D**). Additional stratified correlation analysis after dividing the datasets in low (bottom ⅓), medium (middle ⅓), and high (top ⅓) gene expression, also revealed high correlation scores in the gene expression before and after batch effect correction (**Supplementary Fig. 11D**). Finally, we observe a high correlation of the first principal component of the PCA plot with the main MASLD characteristics without significant association with sex (**Supplementary Fig. 11E,F**), and a similar expression of genes previously linked to MASLD before and after the correction (**Supplementary Fig. 11G**), validating the robustness of the batch effect correction.

Pseudo-temporal ordering of patients

The merged dataset was not expected to have multiple disconnected trajectories with a particular cyclic or (necessarily) complex topology. Thus, we selected *Slingshot*[91,92] as the most suitable tool to infer the disease trajectory. We constructed an MST (Minimum Spanning Tree) on ordered sets of clusters to capture the disease trajectory from points on the PCA plot. The inferred horizontal trajectory was consistent with the high correlation scores between PC1 and the MASLD characteristics and explained 9% of the variance of the scaled and normalised dataset (~55% of the pre-normalised data; **Supplementary Fig. 11A, B**). It did not show any significant correlation with potential confounders, such as age (**Supplementary Fig. 11E**). This validates our design that was intended to capture the common molecular continuum of progression across the cohort, as reflected in the histological phenotypes and independent of variables such as sex or T2DM. Thus, this dimension could be considered as a pseudo-temporal trajectory of MASLD, in which

610 low values correspond to healthy or early disease stages, as reflected in biopsy histopathology,
611 while large values correspond to severe fibrosis conditions. For the independent dataset, this
612 process was repeated using the complete transcriptome and only the 145 gene signatures
613 identified by the random forest classification (see section below). The order of patients in our
614 trajectory is described in **Supplementary Table 1.**

615 Patient stratification for annotation of trajectory

616 Based on the histological scores defined by the CRN scoring system[6] and following the older
617 definition of NAFLD/NASH, our dataset (136 patients) has been divided into 4 bariatric obese
618 controls and 132 MASLD, which has further been sub-clustered based on the fibrosis stage into
619 mild (MASH F0), moderate (MASH F1-2) and severe (MASH F3-4) groups. This stratification aims
620 to increase the interpretability of the analysis, which has been described in detail in our previous
621 studies[33,85] (**Supplementary Table 1**).

622 Extraction of 145 gene signatures using Random Forest classification

623 By calling the parameter *rotation* from *prcomp* function in R (default stats package), we produced
624 a list of ranked genes with the highest absolute values that explain the variance, along with the
625 disease progression on the horizontal axis. The top 200 genes were selected as the training set
626 of a random forest classification model (R package *randomForest*) to predict the disease stage
627 (MASL, MASHF01, MASHF2, MASHF34) and the different MASLD characteristics (steatosis,
628 inflammation, ballooning, fibrosis). The accuracy was estimated using 5-fold cross-validation
629 1000 times. From this first model run, only genes with positive “Mean Decrease Accuracy” were
630 selected, yielding the set of 145 top genes that contributed to disease stage prediction
631 (**Supplementary Table 1**). Those genes were used as the training set of a new random forest
632 classification model. Testing the model on three independent cohorts (GUBRA[34,84], EPoS[13],
633 Fujiwara[35]) conclusively demonstrated its generalisability. **Supplementary Table 3** shows AUC
634 values from ROC plots for two-way classification of the groups, as we cannot generate 3-way
635 classification ROC.

636 Pathway enrichment analysis

637 The Reactome Pathway Knowledgebase[38] (accessed May 2024) was used in different steps of
638 this study to perform pathway enrichment analysis. Fisher's exact test[93] was used for the statistical

639 significance test, and the Benjamini–Hochberg method[94] was applied for the multiple hypothesis
640 testing correction. The KEGG database was used for pathway enrichment analysis of the 145
641 gene signature in Figure 1E to facilitate visualisation, as these pathways are more generic.

642 Identification of gene expression modules associated with MASLD 643 histological phenotypes

644 We performed weighted gene co-expression network analysis (WGCNA)[95], as in Barker et al.[36],
645 using the R package *WGCNA*[37] (v 1.72-1) on the full transcriptome to capture MASLD-related
646 molecular programmes. A signed network was constructed using a soft-thresholding power of 4,
647 the minimum value that achieved an approximate scale-free topology (fit index = 0.9). Adjacency
648 weights were transformed into a topological overlap matrix (TOM), and gene co-expression
649 modules were identified from the resulting dissimilarity matrix (1–TOM) using dynamic tree cutting
650 (function *cutreeDynamic,* package *dynamicTreeCut* v1.63-1).

651 Module–phenotype associations were assessed by linking module eigengenes to histological
652 traits, with inflammation included as a covariate to control for its dominant transcriptomic signal
653 and its ambiguous role as cause versus consequence of disease. As inflammation is incorporated
654 into the NAS score, this approach enables identification of modules specifically associated with
655 steatosis, ballooning, fibrosis, and NAS beyond global inflammatory effects. We also included age
656 as a covariate because it is a well-established determinant of MASLD progression, influencing
657 both hepatic and systemic metabolic states.

658 To optimise module detection, we tuned the *deepSplit* and *minClusterSize* parameters using a
659 cross-validated optimisation strategy. Module eigengenes were evaluated for their ability to model
660 the four MASLD phenotypes using linear regression (*lm* and *step* functions of the *stats* R package)
661 with four-fold cross-validation (*crossv_kfold* function of the *modelr* R package (v 0.1.11)),
662 selecting parameters that maximised predictive performance while adjusting for
663 inflammation.Each linear model had the following format:

664 $$MASLD\ phenotype \sim intercept + eigengenes\ of\ modules + inflammation + age$$

665 We optimised linear models using backward stepwise selection with the Akaike Information
666 Criterion (AIC)[96], retaining only modules with significant coefficients (adjusted $p < 0.05$,
667 Benjamini–Hochberg correction[94]). Model performance was evaluated on held-out test sets using
668 mean squared error (MSE). Average test MSEs across the four MASLD phenotypes were used

669 to identify optimal parameters, resulting in the following parameter settings: *deepSplit* = 4 and
670 *minClusterSize* = 180. Final models were built using these parameters. For the downstream
671 analysis, we filtered the module gene sets based on their Pearson correlation with the
672 corresponding eigengene. For modules with fewer than 1,000 genes, we removed genes with
673 non-positive correlation. For larger modules, we applied a cutoff at the 20th percentile of the
674 correlation scores to exclude genes with lower values (**Supplementary Table 6**).

675 Transcription factor activities analysis

676 We used *VIPER*[97] (Virtual Inference of Protein-activity by Enriched Regulon analysis; v 1.37.0)
677 and the CollecTRI database[98] (accessed May 2024) to identify the upstream transcriptional
678 regulators that can explain the observed gene expression changes. The calculated Normalised
679 Enrichment Score (NES) was used to determine the direction of each regulation ("activation" for
680 TFs with NES > 0 and "inhibition" for those with NES < 0). We performed hypothesis testing using
681 the Student's t-test, and then, the Benjamini-Hochberg method[94] was used to correct the p-values,
682 thereby reducing Type I errors (**Supplementary Tables 8 & 12**).

683 Constructions of global MASLD network

684 To construct a global interaction network capturing molecular processes across MASLD stages,
685 we integrated signalling and transcriptional regulation inferred from WGCNA modules, differential
686 expression, and TF activity across SWs. For each MASLD phenotype, we generated upstream
687 (signalling) and downstream (transcriptional) subnetworks using the *Prize-Collecting Steiner*
688 *Forest* (PCSF) algorithm[99] (*PCSF* R package v0.99.1), and subsequently merged them into a
689 unified MASLD network.

690 *PCSF* returns as output a subset of a given reference network relevant to an input-weighted list
691 of prize-carrying nodes. Prize-carrying nodes were defined from two complementary sources.
692 First, for WGCNA-derived modules, we performed TF enrichment using CollecTRI[98] and TF-
693 regulon databases from *EnrichR*[100] (ENCODE and ChEA Consensus TFs from ChIP-X[101], DNA
694 binding preferences from JASPAR[102,103], TF protein-protein interactions), followed by
695 Reactome[104] pathway enrichment of the enriched TFs to identify semantically specific signalling
696 pathways (**Supplementary Tables 8 and 9**). Filtered module genes (downstream nodes),
697 enriched TFs, and genes from associated Reactome pathways (upstream nodes) constituted the
698 prize-carrying nodes for each MASLD variable.

699 Second, for differentially expressed genes, we selected TFs deregulated in at least one SW (FDR
700 < 0.05; **Supplementary Table 12**), identified their associated signalling pathways
701 (**Supplementary Table 9,** as above), and intersected their regulons (using the CollecTRI
702 annotation[98]) with WGCNA modules. These regulon genes, deregulated TFs, and pathway genes
703 defined the prize-carrying nodes for the deregulated network. All enrichment analyses used
704 Fisher's exact test with Benjamini–Hochberg correction (FDR < 0.05), restricting background
705 genes to those detected in the transcriptomic data.

706 The reference interaction network was assembled by integrating curated signalling and metabolic
707 interactions from Reactome[104], KEGG[105,106], HumanCyc[107], ReconX[108], provided by Pathway
708 Commons[109] (v12), and OmniPath[110], accessed using the *OmniPathR* library (v3.17) in
709 Bioconductor[111,112] and using the *union* function of the *igraph* R package (v 2.03)[113]. Weakly
710 supported OmniPath interactions were removed, keeping only those where the number of
711 resources and curation efforts were above the 0.5 and 0.75 quantiles of their respective
712 distributions. Dead-end metabolites were also excluded, protein complexes were expanded into
713 fully connected subgraphs, and inhibitory edges were discarded. The resulting reference network
714 contained 12,549 nodes and 205,706 edges (**Supplementary Table 19**).

715 PCSF was run using fixed edge costs (0.001) and node prizes (1). For each of the five MASLD
716 variables, upstream and downstream subnetworks were generated and iteratively connected,
717 using a randomized PCSF variant (10 iterations adding random noise) to improve robustness.
718 This gradual generation of the MASLD network was selected to preserve information about the
719 origin of each node and edge. These subnetworks were then merged into a global MASLD
720 network, using the *union* function of the *igraph* R package (v 2.0.3).

721 To refine the network, we retained only functionally annotated genes and weighted edges based
722 on Gene Ontology Biological Process[114] semantic similarity, computed using the *GOSemSim* R
723 package[115] (v 2.26.0) and averaged across Resnik[116], Lin[117] and Wang[118] metrics. Nodes lacking
724 GO annotation were removed, and Laplacian normalisation was applied to reduce hub bias[119].
725 The final MASLD network comprised 7,165 nodes and 69,314 edges (**Supplementary Table 10**).

726 Network relevance was assessed by enrichment against two independent MASLD gene
727 signatures: a literature-curated set (164 genes[83,120–124]; **Supplementary Table 11**) and the
728 WikiPathways MASLD pathway from MSigDB[55] (155 genes; 15-gene overlap). Enrichment
729 significance was evaluated using Fisher's exact test.

Patients' stratification into sliding windows

We divided the ordered samples along the trajectory into sliding windows (SWs), namely a sequence of overlapping groups [SW_1, SW_2,..., SW_X], to investigate how the MASLD molecular profile changes in the pseudo-temporal space. To define an optimal SW configuration, we developed a graph-based optimisation framework that evaluates all possible sequences of SWs given a set of window sizes $S=[S_1,\ldots, S_m]$ and a predefined overlap percentage α between adjacent windows.

In this framework, disease stages are represented as nodes in a directed acyclic graph (DAG), where each node corresponds to a group of samples aligned by pseudo-temporal order. Directed edges connect overlapping windows, ensuring continuity along the trajectory. The objective is to identify a path through this graph that best captures progressive molecular changes by enabling sequential comparisons between adjacent windows. Our method is implemented using a three-step workflow: creating of all potential directed paths of SWs, evaluating and filtering, and finally, selecting the optimal one.

The method begins by ordering the N samples according to their scores on the first principal component (PC1) of the expression data. Based on this ordering, each sample is assigned a unique index $i \in [1, 2,..., N]$. Using these indices, an iterative process is performed to construct a directed acyclic graph (DAG), in which nodes correspond to groups of samples and directed edges represent a valid transition between two overlapping groups. An empty starting node is first created as the origin of all paths in the DAG (**Supplementary Fig. 3A**). In the first iteration, a set of nodes is generated using a predefined collection of window sizes $S\in [S_1,\ldots, S_m]$. For each window size S_i a node is created that contains the first Si samples (indices 1 through Si). These nodes constitute the candidate versions of SW_1. Directed edges from the starting node to the SW_1 nodes are created. In subsequent iterations, each existing SW node is extended forward along the index order to generate candidate nodes for the next SW. For a SW node with K samples, the starting index of its subsequent SW nodes is defined as $K+1-ceiling(K*\alpha)$, where α controls the degree of overlap between consecutive windows and ensures that the last $100\alpha\%$ percent of the samples in the current SW will also be included in the next window. New directed edges connect the current node with its subsequent ones. This iterative growth of the graph terminates when all the samples have been mapped to SW nodes. Many nodes and edges could be generated

760 multiple times through the expansion of different paths. Thus, filtering is performed at the end of
761 each iteration to remove this redundancy. Finally, an empty ending node is created and connected
762 with the final SW nodes. All directed paths connecting the starting and ending nodes constitute
763 potential representations of the pseudo-temporal sequence of disease stages (**Supplementary**
764 **Fig. 3A**).

765 To evaluate candidate paths, we performed differential expression analysis between each pair of
766 adjacent SWs using DESeq2[125]. Edges were initially retained if the number of differentially
767 expressed genes (DEGs; FDR < 0.1) fell within an empirically defined range *R=[100, 1000]*,
768 reflecting sufficiently strong but not excessive differentiation (that would be best captured in more
769 than two SWs). Graph evaluation proceeded iteratively. To reduce computational burden, paths
770 containing edges outside this range were pruned at each iteration. To preserve graph
771 connectivity, DEG thresholds (i.e. the range of *R*) were adaptively relaxed such that the lower
772 bound did not exceed the 80th percentile and the upper bound did not fall below the 20th
773 percentile of the observed DEG distribution.

774 This procedure typically yielded multiple candidate paths. Additional filtering was applied to select
775 the optimal one. First, incoming edges to each SW node were clustered by the upstream node's
776 starting index, retaining only the edge with the highest DEG count (or, if tied, the one spanning
777 more samples). Second, edges below the lower DEG threshold were used to compute a median
778 DEG value, and edges with fewer DEGs were removed while preserving graph connectivity
779 (**Supplementary Fig. 3B**). Remaining paths were ranked using the product of three max-scaled
780 criteria: (i) median DEG count, (ii) number of edges exceeding the lower DEG threshold, and (iii)
781 coefficient of variation of DEG counts along the path, using the following pairs of SW sizes and
782 overlap scores: ([6,15], 0.2), ([8,17], 0.25), ([8,24], 0.3), ([10,20], 0.3), ([12,25], 0.35). Therefore,
783 five graphs were constructed and filtered, and the candidate paths from all of them were prioritized
784 to find the optimal SW sequence (**Supplementary Fig. 3C**; **Supplementary Table 5**).

785 Statistical analysis

786 Differential gene expression analysis was done using *DESeq2*[125] (v 1.26.0), and the Benjamini-
787 Hochberg method was applied to adjust the raw p-values to control the False Discovery Rate
788 (FDR). In analyses using discrete stratification of patients' disease stages, comparisons were
789 made to the immediately preceding stage. For all comparisons related to the trajectory analysis

(see section “Patients stratification into sliding windows”), sliding windows (SWs) were compared to the previous SW (SW_x vs SW_{x-1}).

Disease stage-specific network analysis

We applied a network propagation-based approach to detect the deregulated components of the MASLD network for each SW using the *igraph* R package (v 2.0.3). We used the personalised *PageRank* algorithm[126] to run network propagation. This method accepts a vector of weights for a set of nodes as input. We defined these weights based on results from differential expression analysis (for all genes except transcription factors) and TF activity analysis (for transcription factors). We were interested in finding a network signature for up- and down-regulated conditions separately, so we created two weight vectors for each SW. In particular, we defined the weights of node i (W_+ and W_-) using the direction of its differentiation (based on the logarithmic fold change or NES score) and the log-transformed adjusted p-value of the respective statistical test, to be bounded by a maximum value of 10:

- $If\ sign(deregulation) = +1: Weights_i : \{W_+ = min[-log_{10}(adj.pvalue) + 1, 10],\ W_- = 1\}$
- $If\ sign(deregulation) = -1: Weights_i : \{W_+ = 1,\ W_- = min[-log_{10}(adj.pvalue) + 1, 10]\}$

Network propagation was performed for each SW and direction of deregulation. To assess the statistical significance of the derived PageRank scores, we run the propagation task 1000 times using random weight distributions. Then, we calculated an empirical p-value for each node based on the ratio of its random scores that are lower than the real one:

$$pvalue = 1 - \frac{|random\ scores\ < PageRank\ score|}{1000}$$

We implemented this approach for three values of the damping factor: [0.5, 0.7, 0.85], and we selected the gene nodes with p-value<0.05 in all three runs as significantly propagated. Then, we extracted the respective subnetwork signature as a subgraph of the MASLD network and we removed the isolated nodes, keeping only the components with two or more members. Finally, the activation score of a gene in a SW was defined as the average of the log-transformed empirical p-values obtained from the network propagation runs using the three damping factors.

Definition of disease-relevant pathways

We used pathway enrichment analysis to link deregulated subnetworks in each SW to molecular pathways using Reactome[38] (see "Pathway enrichment analysis"; **Supplementary Table 13**). This analysis yields distinct sets of significantly enriched pathways (terms) for each SW and each direction of deregulation. To extract a unified, comprehensive set of MASLD-relevant pathways with minimal semantic redundancy, we created a slim version of Reactome by pruning its hierarchical structure. We finally project all the enriched terms on that slim graph.

First, we constructed the Reactome graph using the *igraph* Python package (v 0.4.11), to encode parent–child semantic relationships. We calculated the information content[116] (IC) and semantic value[127] (SV) of Reactome terms using their reference genomic annotations. These two properties capture the specificity of terms within the graph, with higher values corresponding to more semantically specific terms. Firstly, we retained the most generic terms by filtering out those above the 25th percentile of each distribution. This filtering step reduced the number of Reactome terms from 2,655 to 315. Secondly, we examined the semantic distances between the leaf terms of the pruned graph and their parents terms, by calculating the differences of their IC and SV values. If both distances were lower than the median values of respective distributions and the parent term was not a direct child of the graph root, then the child terms were filtered out, as they were considered semantically similar to their parent. This step defined the final slim version of Reactome, which consisted of 225 terms (**Supplementary Table 20**).

To define the list of MASLD-related pathways, we used the Reactome slim graph as a framework. We first performed Reactome enrichment analysis on the global MASLD network (FDR < 0.05) and intersected the enriched terms with those in the graph. This resulting subgraph was used as a reference to filter the SW-level enriched pathways (FDR < 0.05). For each set of enriched pathways, we checked whether they were present in the reference subgraph or could be mapped to ancestral terms within it. Enriched terms that failed to be mapped to the reference subgraph were removed. Additionally, terms with fewer than 10 genes in the respective SW-based deregulated subnetworks were removed as they were considered highly specific for the comprehensive set of MASLD-related pathways. This filtering step created a MASLD-related subgraph of Reactome with 141 pathways (**Supplementary Table 20**). Finally, we selected the leaf terms of that subgraph, along with their parental terms if they were not directly linked to the root and the annotations of their child terms did not capture more than 20% of their genomic

848 annotations in the deregulated networks. This final step defined a list of 111 MASLD-related
849 pathways (**Supplementary Fig. 6**; **Supplementary Table 13**).

850 To calculate the activation scores of the MASLD-related pathways along the disease trajectory,
851 we used the activation scores of their related genes sets ((see "Disease stage-specific network
852 analysis"). We created a subnetwork for each pathway, intersecting the global MASLD network
853 and their reference gene sets. The activation scores of each pathway for a specific SW was
854 defined as the summation of the activation scores of its related genes in that SW, normalised by
855 their pagerank centralities[126] on the pathway-based subnetwork. The respective cumulative
856 scores were defined by progressively summing the SW-based activation scores (**Supplementary**
857 **Fig. 6**; **Supplementary Table 13**).

858 Cell-type deconvolution analysis

859 As a reference for the deconvolution analysis, we used the Liver Cell Atlas, a 10X single-cell RNA-
860 seq dataset from a healthy human liver[68]. We re-analysed the single-cell dataset following
861 standard single-cell analysis workflows[128]. Genes expressed in fewer than three cells and cells
862 expressing fewer than 200 genes were removed. Cells with more than 7,000 detected features
863 (putative doublets) or with >5% mitochondrial gene content were also excluded. The filtered data
864 were then normalised and variance-stabilised, followed by identification of highly variable genes
865 (HVGs), principal component analysis (PCA), and UMAP dimensionality reduction to assess data
866 structure and suitability for downstream analyses.

867 For the deconvolution analysis, we applied the CATD pipeline[129], using the raw counts as input.
868 CATD performs normalisation and additional preprocessing internally. After setting the
869 preprocessing parameters, we run the deconvolution analysis, selecting a subset of methods
870 (EpiDISH[130], bseqsc[131], DWLS[132], CIBERSORT[133], FARDEEP[134] and BayesPrism[135]). The
871 consensus result was calculated as the mean of cell-type proportion per cell-type across methods
872 (**Supplementary Table 14**). We used these methods to calculate the consensus cell type
873 proportions because they ranked among the top-10 of the 31 deconvolution methods of the CATD
874 pipeline across multiple metrics, based on benchmarking on real bulk RNA-seq samples[129].

875

876

Identification of cell-type specific deregulated pathways

We assumed that differentiated network signatures arise from either shifts in cell-type composition or from deregulation of cell-intrinsic biological processes. To disentangle these effects and identify pathway deregulation attributable to specific cell types, we applied the following workflow:

Initially, using patient stratification into SWs and the corresponding cell-type proportions (see “Cell type deconvolution analysis”), we modeled Gaussian kernel density functions for cell-type proportions within each SW. These kernels were used to generate pseudo-bulk RNA-seq samples by sampling cells from a healthy liver single-cell reference dataset[68], with predefined library sizes. For each SW, the number of pseudo-samples (6–20) and library sizes (20–50 million counts) were randomly selected. Differential expression, TF activity, and network-based analyses were then performed on these pseudo-datasets using the same pipeline as for the real data, under the assumption that the resulting signatures reflect network differentiation driven solely by changes in cell-type composition. We generated 30 pseudo-datasets and averaged differential expression and TF activity results across replicates.

Network analysis of the pseudo-datasets yielded up- and down-regulated components, which were compared with the corresponding real SW signatures. Genes present in both real and pseudo signatures, whose activation score in the pseudo-signature exceeded that in the real signature, were classified as composition-driven and removed from MASLD-relevant pathways (see “Definition of disease-relevant pathways”). The remaining genes were therefore assumed to reflect pathway deregulation independent of changes in cell-type proportions.

To assess whether deregulated pathways were associated with specific liver cell types, we first derived extended cell-type marker sets from the reference single-cell dataset using the *Seurat* R package (v. 5.0.3)[136]. Marker lists were filtered to retain only genes present in the global MASLD network. Each marker set was then expanded using the PCSF algorithm (with the same parameters as in “Generation of global MASLD network”; *PCSF* R package v0.99.1) to incorporate topologically proximal genes from the MASLD network and amplify each gene set. Finally, enrichment analysis was performed to evaluate the association between deregulated pathways and cell types using Fisher’s exact test, with Benjamini–Hochberg correction for multiple testing (FDR<0.05; **Supplementary Table 15**).

907 # Machine Learning Models for Non-Invasive MASLD Biomarker Prediction

908 **Random forest classification for fibrosis stage prediction**

909 Govaere et al, identified a set of 194 genes whose gene expression in the liver correlated with
910 that at the proteome plasma level[69]. In brief the data for this study came from 191 histologically
911 characterized NAFLD cases collected across six European specialist centres participating in the
912 European NAFLD Registry (NCT04442334), encompassing fibrosis stages F0–F4 and centrally
913 scored using the NASH-CRN system. Protein quantification was performed using the SomaScan
914 aptamer-based platform (SomaLogic).

915 From this set, we derived a curated panel of 57 biomarker genes by intersecting the 194 genes
916 with the differentiated component of our global MASLD network. A random forest classifier was
917 trained to distinguish early (F0-F2) from advanced fibrosis (F3-F4). Training was performed on
918 the UCAM/VCU internal cohort using 5-fold cross validation across 1000 iterations to ensure
919 model stability. Gene-importance scores were extracted, and the “elbow” method was applied to
920 select a subset of 15 genes above the inflection point. A second classifier was trained using this
921 gene subset.

922 Performance was assessed using ROC analysis, area under the curve (AUC), sensitivity,
923 specificity, and overall accuracy as evaluation metrics. External validation was performed on the
924 EPoS[13] and Fujiwara[35] datasets, with the classifier trained exclusively on the UCAM/VCU dataset
925 and applied to those two external datasets without retraining. For benchmarking, we directly
926 compared its performance with commonly used non-invasive fibrosis scores used in clinical
927 practice, including FIB-4, APRI, and NFS (when available). To assess model robustness we
928 generated 300 random 57-gene sets and compared their AUC distributions with that of our
929 curated 57-gene panel.

930 To test translatability from transcriptomics to proteomics, we applied the trained model to the
931 plasma proteomics measurements from Govaere et al [69]. The same 57-gene (protein) signature
932 was used, and corresponding protein abundance was z-score-scaled prior to prediction. Model
933 predictions were compared to patient fibrosis stages (F0–F2 vs F3–F4) using ROC analysis. The
934 resulting AUC, sensitivity, and specificity were calculated at the optimal threshold determined by
935 Youden’s J index. We acknowledge that the plasma proteomics data were taken from Govaere
936 et al.[69], who identified liver–plasma correlated proteins; however, no feature selection or model

training was performed on these data. All model development was carried out exclusively in independent liver transcriptomic cohorts, with proteomics used only to assess cross-omic translatability rather than independent discovery or validation.

Random forest regression for trajectory position prediction

To predict each patient's position along the MASLD trajectory, we developed Random Forest regression models trained using our 57- and 15-gene signatures, respectively. For each model, the data were randomly split into training (80%) and testing (20%) sets, and performance was evaluated across 1000 iterations by calculating the mean R^2 and its corresponding p-value (Pearson correlation between full-transcriptome trajectory positions and predictions based on the 57 or 15 gene sets).

Expression data were transformed into z-scores based on the 194 gene set (194 plasma proteins correlated with liver transcriptomics according to the proteomics study from Govaere et al[69]). This approach ensures predictions even when partial proteomic measurements are available, enabling potential real-time prediction of patients' position on our trajectory based solely on the most informative plasma proteins.

The same regression models were applied on two independent transcriptomic datasets (Gubra and EPoS) and to the Govaere plasma proteomics dataset[69], using the UCAM/VCU model for training and the external datasets exclusively for testing. Generalisability was confirmed by comparing predicted vs reference trajectory positions. Random 57-gene sets were used as negative controls, evaluated over 300 runs per dataset, with predictive metrics averaged, highlighting the predictive value of our selected gene signature.

GWAS Catalog mining and trait categorisation

The GWAS Catalog (v1.0)[70] was used to extract all associations between our selected biomarkers and traits (**Supplementary Table 16**). For each gene, all associated GWAS traits were aggregated into biologically interpretable categories using regular expressions. The predefined categories were: Metabolic, Liver, Cardiovascular, Inflammatory, Neurological, and Cancer, while traits that did not match any of these were assigned to "Other". The number of unique genes per category was calculated and visualised using bar plots. Genes mapped to multiple categories were identified and reported separately. Gene–trait relationships were visualised using a dot plot,

illustrating the breadth of cross-system associations. To test whether specific trait categories were overrepresented among the 57 MASLD biomarkers relative to the background set of all genes reported in the GWAS Catalog, Fisher's tests were performed per category. Finally, p-values were adjusted using the Benjamini–Hochberg method (FDR < 0.05).

Mapping of small molecules onto biomarker panel

To identify potential candidate small molecules that can be used to target our biomarkers we searched in the ChEMBL database[137] for approved or clinical candidate drugs (max_phase : [2,3,4]) that target these genes. Each biomarker had been identified as up- or down-regulated in specific SWs based on our network analysis. We therefore searched for drugs whose action potentially inverses the deregulation of the respective targets (agonists/activators for the down-regulated and inhibitors/antagonists for the up-regulated genes). Finally, we created a mapping of drugs and drug targets for molecular events related to the 10 biomarkers for which small molecules targeting them existed in the database (**Supplementary Table 17**).

Data and code availability

All data used in this study are publicly available as described in the methods. The code used for the analyses can be found here: https://github.com/kamzolas/MASLD---Continuous-trajectory-approach

Acknowledgements

The work was supported by the European Molecular Biology Laboratory (IK, TK, CGB, AVP, IP, HW, EP) and Open Targets (TK, IP, EP); The EMBL GeneCore Facility is acknowledged for support in transcriptomics data collection. EMBL IT Support is acknowledged for the provision of computer and data storage servers. Funding from the Medical Research Council (MRC) and the NIHR Cambridge Biomedical Research Centre (NIHR203312) supported I. Kamzolas. MRC MDU, Caixa Foundation and Spanish Government ATRAE programme support AVP research on MASLD.

992 # Author contributions

993 IK, TK: Conceptualization, Methodology, Software, Validation, Formal analysis, Investigation,
994 Data curation, Writing - Original Draft, Writing - Review & Editing, Visualisation. CGB, AVP:
995 Formal analysis, Investigation, HW: Data Curation, MV: Writing - Review & Editing, Supervision,
996 NF, YH, QMA: Resources, IP: Supervision, Funding acquisition, AVP: Conceptualization,
997 Supervision, Resources, Funding acquisition, Writing - Review & Editing EP: Conceptualization,
998 Methodology, Resources, Supervision, Project administration, Visualisation, Funding acquisition,
999 Writing - Original Draft, Writing - Review & Editing.

1000 # References

1001 1. Chan, W. K. *et al.* Metabolic Dysfunction-Associated Steatotic Liver Disease (MASLD): A
1002 State-of-the-Art Review. *Journal of obesity & metabolic syndrome* **32**, (2023).
1003 2. Loomba, R. & Sanyal, A. J. The global NAFLD epidemic. *Nat. Rev. Gastroenterol. Hepatol.*
1004 **10**, (2013).
1005 3. Estes, C. *et al.* Modeling NAFLD disease burden in China, France, Germany, Italy, Japan,
1006 Spain, United Kingdom, and United States for the period 2016-2030. *J. Hepatol.* **69**, (2018).
1007 4. Angulo, P. *et al.* The NAFLD fibrosis score: a noninvasive system that identifies liver fibrosis
1008 in patients with NAFLD. *Hepatology (Baltimore, Md.)* **45**, (2007).
1009 5. Sterling, R. K. *et al.* Development of a simple noninvasive index to predict significant fibrosis
1010 in patients with HIV/HCV coinfection. *Hepatology* **43**, 1317–1325 (2006).
1011 6. Kleiner, D. E. *et al.* Design and validation of a histological scoring system for nonalcoholic
1012 fatty liver disease. *Hepatology* **41**, 1313–1321 (2005).
1013 7. McGill, D. B., Rakela, J., Zinsmeister, A. R. & Ott, B. J. A 21-year experience with major
1014 hemorrhage after percutaneous liver biopsy. *Gastroenterology* **99**, (1990).
1015 8. Ratziu, V. *et al.* Sampling variability of liver biopsy in nonalcoholic fatty liver disease.
1016 *Gastroenterology* **128**, (2005).
1017 9. Chalasani, N. *et al.* The diagnosis and management of nonalcoholic fatty liver disease:
1018 Practice guidance from the American Association for the Study of Liver Diseases. *Hepatology*
1019 *(Baltimore, Md.)* **67**, (2018).
1020 10. EASL-EASD-EASO Clinical Practice Guidelines on the management of metabolic
1021 dysfunction-associated steatotic liver disease (MASLD). *Journal of hepatology* **81**, (2024).
1022 11. Castera, L., Forns, X. & Alberti, A. Non-invasive evaluation of liver fibrosis using transient

1023 elastography. *Journal of hepatology* **48**, (2008).
1024 12. Bedossa, P. Utility and appropriateness of the fatty liver inhibition of progression (FLIP)
1025 algorithm and steatosis, activity, and fibrosis (SAF) score in the evaluation of biopsies of
1026 nonalcoholic fatty liver disease. *Hepatology (Baltimore, Md.)* **60**, (2014).
1027 13. Govaere, O. *et al.* Transcriptomic profiling across the nonalcoholic fatty liver disease
1028 spectrum reveals gene signatures for steatohepatitis and fibrosis. *Sci. Transl. Med.* **12**,
1029 (2020).
1030 14. Hoang, S. A. *et al.* Gene Expression Predicts Histological Severity and Reveals Distinct
1031 Molecular Profiles of Nonalcoholic Fatty Liver Disease. *Sci. Rep.* **9**, 12541 (2019).
1032 15. Atabaki-Pasdar, N. *et al.* Predicting and elucidating the etiology of fatty liver disease: A
1033 machine learning modeling and validation study in the IMI DIRECT cohorts. *PLoS Med.* **17**,
1034 e1003149 (2020).
1035 16. Anstee, Q. M., Seth, D. & Day, C. P. Genetic Factors That Affect Risk of Alcoholic and
1036 Nonalcoholic Fatty Liver Disease. *Gastroenterology* **150**, (2016).
1037 17. Wong, V. W.-S., Adams, L. A., de Lédinghen, V., Wong, G. L.-H. & Sookoian, S. Noninvasive
1038 biomarkers in NAFLD and NASH - current progress and future promise. *Nat. Rev.*
1039 *Gastroenterol. Hepatol.* **15**, 461–478 (2018).
1040 18. Eslam, M. & George, J. Genetic contributions to NAFLD: leveraging shared genetics to
1041 uncover systems biology. *Nat. Rev. Gastroenterol. Hepatol.* **17**, 40–52 (2019).
1042 19. Chen, Y. *et al.* Genome-wide association meta-analysis identifies 17 loci associated with
1043 nonalcoholic fatty liver disease. *Nat. Genet.* **55**, 1640–1650 (2023).
1044 20. Fairfield, C. J. *et al.* Genome-Wide Association Study of NAFLD Using Electronic Health
1045 Records. *Hepatology Communications* **6**, 297 (2022).
1046 21. Genome-wide association study of non-alcoholic fatty liver and steatohepatitis in a
1047 histologically characterised cohort☆. *J. Hepatol.* **73**, 505–515 (2020).
1048 22. Romeo, S. *et al.* Genetic variation in PNPLA3 confers susceptibility to nonalcoholic fatty liver
1049 disease. *Nature Genetics* **40**, 1461–1465 (2008).
1050 23. Rotman, Y., Koh, C., Zmuda, J. M., Kleiner, D. E. & Liang, T. J. The association of genetic
1051 variability in patatin-like phospholipase domain-containing protein 3 (PNPLA3) with
1052 histological severity of nonalcoholic fatty liver disease. *Hepatology (Baltimore, Md.)* **52**,
1053 (2010).
1054 24. Kozlitina, J. *et al.* Exome-wide association study identifies a TM6SF2 variant that confers
1055 susceptibility to nonalcoholic fatty liver disease. *Nature genetics* **46**, (2014).

1056 25. Mancina, R. M. *et al.* The MBOAT7-TMC4 Variant rs641738 Increases Risk of Nonalcoholic
1057 Fatty Liver Disease in Individuals of European Descent. *Gastroenterology* **150**, (2016).
1058 26. Abul-Husn, N. S. *et al.* A Protein-Truncating HSD17B13 Variant and Protection from Chronic
1059 Liver Disease. *New England Journal of Medicine* (2018) doi:10.1056/NEJMoa1712191.
1060 27. Magwene, P. M., Lizardi, P. & Kim, J. Reconstructing the temporal ordering of biological
1061 samples using microarray data. *Bioinformatics* **19**, 842–850 (2003).
1062 28. Mukherjee, S. *et al.* Molecular estimation of neurodegeneration pseudotime in older brains.
1063 *Nat. Commun.* **11**, 5781 (2020).
1064 29. Young, A. L. *et al.* Data-driven modelling of neurodegenerative disease progression: thinking
1065 outside the black box. *Nat. Rev. Neurosci.* **25**, 111–130 (2024).
1066 30. Cherubini, A., Della Torre, S., Pelusi, S. & Valenti, L. Sexual dimorphism of metabolic
1067 dysfunction-associated steatotic liver disease. *Trends in molecular medicine* **30**, (2024).
1068 31. Glass, L. M., Hunt, C. M., Fuchs, M. & Su, G. L. Comorbidities and Nonalcoholic Fatty Liver
1069 Disease: The Chicken, the Egg, or Both? *Federal Practitioner* **36**, 64 (2019).
1070 32. Rosato, V. *et al.* NAFLD and Extra-Hepatic Comorbidities: Current Evidence on a Multi-Organ
1071 Metabolic Syndrome. *International Journal of Environmental Research and Public Health* **16**,
1072 3415 (2019).
1073 33. Azzu, V. *et al.* Suppression of insulin-induced gene 1 (INSIG1) function promotes hepatic
1074 lipid remodelling and restrains NASH progression. *Molecular metabolism* **48**, (2021).
1075 34. Suppli, M. P. *et al.* Hepatic transcriptome signatures in patients with varying degrees of
1076 nonalcoholic fatty liver disease compared with healthy normal-weight individuals. *Am. J.*
1077 *Physiol. Gastrointest. Liver Physiol.* **316**, (2019).
1078 35. Fujiwara, N. *et al.* Molecular signatures of long-term hepatocellular carcinoma risk in
1079 nonalcoholic fatty liver disease. *Science translational medicine* **14**, (2022).
1080 36. Barker, C. G. *et al.* Identification of phenotype-specific networks from paired gene
1081 expression–cell shape imaging data. *Genome Res.* **32**, 750 (2022).
1082 37. Langfelder, P. & Horvath, S. WGCNA: an R package for weighted correlation network
1083 analysis. *BMC Bioinformatics* **9**, 1–13 (2008).
1084 38. Milacic, M. *et al.* The Reactome Pathway Knowledgebase 2024. *Nucleic Acids Res.* **52**,
1085 D672–D678 (2023).
1086 39. Maiers, J. L. & Malhi, H. Endoplasmic Reticulum Stress in Metabolic Liver Diseases and
1087 Hepatic Fibrosis. *Seminars in liver disease* **39**, (2019).
1088 40. Ortiz, C. *et al.* Extracellular Matrix Remodeling in Chronic Liver Disease. *Current tissue*

1089 *microenvironment reports* **2**, (2021).
1090 41. Nassir, F. NAFLD: Mechanisms, Treatments, and Biomarkers. *Biomolecules* **12**, (2022).
1091 42. Córdova, G. *et al.* SMAD3 and SP1/SP3 Transcription Factors Collaborate to Regulate
1092 Connective Tissue Growth Factor Gene Expression in Myoblasts in Response to
1093 Transforming Growth Factor β. *J. Cell. Biochem.* **116**, 1880–1887 (2015).
1094 43. Younesi, F. S., Miller, A. E., Barker, T. H., Rossi, F. M. V. & Hinz, B. Fibroblast and
1095 myofibroblast activation in normal tissue repair and fibrosis. *Nat. Rev. Mol. Cell Biol.* **25**, 617–
1096 638 (2024).
1097 44. Liu, D. *et al.* Ets-1 deficiency alleviates nonalcoholic steatohepatitis via weakening TGF-β1
1098 signaling-mediated hepatocyte apoptosis. *Cell Death Dis.* **10**, 1–14 (2019).
1099 45. Varga, T., Czimmerer, Z. & Nagy, L. PPARs are a unique set of fatty acid regulated
1100 transcription factors controlling both lipid metabolism and inflammation. *Biochim. Biophys.*
1101 *Acta* **1812**, 1007 (2011).
1102 46. Vachliotis, I. D. & Polyzos, S. A. The Role of Tumor Necrosis Factor-Alpha in the
1103 Pathogenesis and Treatment of Nonalcoholic Fatty Liver Disease. *Curr. Obes. Rep.* **12**, 191–
1104 206 (2023).
1105 47. Tumor necrosis factor-α signaling in nonalcoholic steatohepatitis and targeted therapies. *J.*
1106 *Genet. Genomics* **49**, 269–278 (2022).
1107 48. Parviz, F. *et al.* Hepatocyte nuclear factor 4α controls the development of a hepatic epithelium
1108 and liver morphogenesis. *Nature Genetics* **34**, 292–296 (2003).
1109 49. Tontonoz, P. & Spiegelman, B. M. Fat and beyond: the diverse biology of PPARgamma.
1110 *Annual review of biochemistry* **77**, (2008).
1111 50. Bitter, A. *et al.* Human sterol regulatory element-binding protein 1a contributes significantly
1112 to hepatic lipogenic gene expression. *Cellular physiology and biochemistry : international*
1113 *journal of experimental cellular physiology, biochemistry, and pharmacology* **35**, (2015).
1114 51. Luedde, T. & Schwabe, R. F. NF-κB in the liver—linking injury, fibrosis and hepatocellular
1115 carcinoma. *Nat. Rev. Gastroenterol. Hepatol.* **8**, 108 (2011).
1116 52. Luo, M., Li, T. & Sang, H. The role of hypoxia-inducible factor 1α in hepatic lipid metabolism.
1117 *J. Mol. Med.* **101**, 487–500 (2023).
1118 53. Mesarwi, O. A. *et al.* Hepatocyte Hypoxia Inducible Factor-1 Mediates the Development of
1119 Liver Fibrosis in a Mouse Model of Nonalcoholic Fatty Liver Disease. *PLoS One* **11**,
1120 e0168572 (2016).
1121 54. CREB family: A significant role in liver fibrosis. *Biochimie* **163**, 94–100 (2019).

1122 55. The Molecular Signatures Database Hallmark Gene Set Collection. *Cell Systems* **1**, 417–425
1123 (2015).
1124 56. Browning, J. D. & Horton, J. D. Molecular mediators of hepatic steatosis and liver injury. *J*
1125 *Clin Invest* **114**, 147–152 (2004).
1126 57. Nagaya, T. *et al.* Down-regulation of SREBP-1c is associated with the development of
1127 burned-out NASH. *Journal of hepatology* **53**, (2010).
1128 58. Xu, Y. *et al.* Hepatocyte Nuclear Factor 4α Prevents the Steatosis-to-NASH Progression by
1129 Regulating p53 and Bile Acid Signaling (in mice). *Hepatology* **73**, 2251–2265 (2021).
1130 59. Maglich, J. M., Lobe, D. C. & Moore, J. T. The nuclear receptor CAR (NR1I3) regulates serum
1131 triglyceride levels under conditions of metabolic stress. *Journal of lipid research* **50**, (2009).
1132 60. Tan, J. *et al.* HNF1α Controls Liver Lipid Metabolism and Insulin Resistance via Negatively
1133 Regulating the SOCS-3-STAT3 Signaling Pathway. *Journal of Diabetes Research* **2019**,
1134 5483946 (2019).
1135 61. Zhang, S. *et al.* Smad7 Antagonizes Transforming Growth Factor β Signaling in the Nucleus
1136 by Interfering with Functional Smad-DNA Complex Formation. *Molecular and Cellular Biology*
1137 **27**, 4488 (2007).
1138 62. Lu, J., McKinsey, T. A., Zhang, C. L. & Olson, E. N. Regulation of skeletal myogenesis by
1139 association of the MEF2 transcription factor with class II histone deacetylases. *Mol. Cell* **6**,
1140 (2000).
1141 63. Mann, D. A. & Smart, D. E. Transcriptional regulation of hepatic stellate cell activation. *Gut*
1142 **50**, 891 (2002).
1143 64. Schüler, A. *et al.* The MADS transcription factor Mef2c is a pivotal modulator of myeloid cell
1144 fate. *Blood* **111**, 4532–4541 (2008).
1145 65. Cilenti, F. *et al.* A PGE2-MEF2A axis enables context-dependent control of inflammatory
1146 gene expression. *Immunity* **54**, (2021).
1147 66. Liu, N. *et al.* Notch and retinoic acid signals regulate macrophage formation from
1148 endocardium downstream of Nkx2-5. *Nature Communications* **14**, 5398 (2023).
1149 67. Mu, W. *et al.* Potential Nexus of Non-alcoholic Fatty Liver Disease and Type 2 Diabetes
1150 Mellitus: Insulin Resistance Between Hepatic and Peripheral Tissues. *Front. Pharmacol.* **9**,
1151 430129 (2019).
1152 68. Guilliams, M. *et al.* Spatial proteogenomics reveals distinct and evolutionarily conserved
1153 hepatic macrophage niches. *Cell* **185**, (2022).
1154 69. Govaere, O. *et al.* A proteo-transcriptomic map of non-alcoholic fatty liver disease signatures.

1155 *Nature Metabolism* **5**, 572 (2023).
1156 70. Buniello, A. *et al.* The NHGRI-EBI GWAS Catalog of published genome-wide association
1157 studies, targeted arrays and summary statistics 2019. *Nucleic acids research* **47**, (2019).
1158 71. Chitturi, S. *et al.* The Asia-Pacific Working Party on Non-alcoholic Fatty Liver Disease
1159 guidelines 2017-Part 2: Management and special groups. *J. Gastroenterol. Hepatol.* **33**,
1160 (2018).
1161 72. Wnt/beta-catenin signaling and its modulators in nonalcoholic fatty liver diseases.
1162 *Hepatobiliary Pancreat. Dis. Int* **22**, 333–345 (2023).
1163 73. Ying, H.-Z. *et al.* PDGF signaling pathway in hepatic fibrosis pathogenesis and therapeutics.
1164 *Mol. Med. Rep.* **16**, 7879 (2017).
1165 74. TGF-β1 signaling can worsen NAFLD with liver fibrosis backdrop. *Exp. Mol. Pathol.* **124**,
1166 104733 (2022).
1167 75. Gribben, C. *et al.* Acquisition of epithelial plasticity in human chronic liver disease. *Nature*
1168 **630**, 166–173 (2024).
1169 76. Vonderlin, J., Chavakis, T., Sieweke, M. & Tacke, F. The Multifaceted Roles of Macrophages
1170 in NAFLD Pathogenesis. *Cell Mol Gastroenterol Hepatol* **15**, 1311–1324 (2023).
1171 77. Matchett, K. P., Paris, J., Teichmann, S. A. & Henderson, N. C. Spatial genomics: mapping
1172 human steatotic liver disease. *Nat. Rev. Gastroenterol. Hepatol.* 1–15 (2024).
1173 78. Harrison, S. A. *et al.* A blood-based biomarker panel (NIS4) for non-invasive diagnosis of
1174 non-alcoholic steatohepatitis and liver fibrosis: a prospective derivation and global validation
1175 study. *The lancet. Gastroenterology & hepatology* **5**, (2020).
1176 79. Levy, M. T., McCaughan, G. W., Marinos, G. & Gorrell. Intrahepatic expression of the hepatic
1177 stellate cell marker fibroblast activation protein correlates with the degree of fibrosis in
1178 hepatitis C virus infection. *Liver* **22**, (2002).
1179 80. Yang, A. T. *et al.* Fibroblast Activation Protein Activates Macrophages and Promotes
1180 Parenchymal Liver Inflammation and Fibrosis. *Cellular and molecular gastroenterology and*
1181 *hepatology* **15**, (2023).
1182 81. Kozumi, K. *et al.* Transcriptomics Identify Thrombospondin-2 as a Biomarker for NASH and
1183 Advanced Liver Fibrosis. *Hepatology (Baltimore, Md.)* **74**, (2021).
1184 82. Lee, C. H. *et al.* Circulating Thrombospondin-2 as a Novel Fibrosis Biomarker of Nonalcoholic
1185 Fatty Liver Disease in Type 2 Diabetes. *Diabetes care* **44**, (2021).
1186 83. Friedman, S. L., Neuschwander-Tetri, B. A., Rinella, M. & Sanyal, A. J. Mechanisms of
1187 NAFLD development and therapeutic strategies. *Nat. Med.* **24**, 908–922 (2018).

1188 84. Heebøll, S. *et al.* Placebo-controlled, randomised clinical trial: high-dose resveratrol
1189 treatment for non-alcoholic fatty liver disease. *Scand. J. Gastroenterol.* (2016)
1190 doi:10.3109/00365521.2015.1107620.
1191 85. Vacca, M. *et al.* An unbiased ranking of murine dietary models based on their proximity to
1192 human metabolic dysfunction-associated steatotic liver disease (MASLD). *Nature*
1193 *Metabolism* **6**, 1178–1196 (2024).
1194 86. Wai, C. T. *et al.* A simple noninvasive index can predict both significant fibrosis and cirrhosis
1195 in patients with chronic hepatitis C. *Hepatology (Baltimore, Md.)* **38**, (2003).
1196 87. Kim, D., Langmead, B. & Salzberg, S. L. HISAT: a fast spliced aligner with low memory
1197 requirements. *Nat. Methods* **12**, 357–360 (2015).
1198 88. Anders, S., Pyl, P. T. & Huber, W. HTSeq—a Python framework to work with high-throughput
1199 sequencing data. *Bioinformatics* **31**, 166–169 (2014).
1200 89. Durinck, S., Spellman, P. T., Birney, E. & Huber, W. Mapping identifiers for the integration of
1201 genomic datasets with the R/Bioconductor package biomaRt. *Nat. Protoc.* **4**, (2009).
1202 90. Zhang, Y., Jenkins, D. F., Manimaran, S. & Johnson, W. E. Alternative empirical Bayes
1203 models for adjusting for batch effects in genomic studies. *BMC Bioinformatics* **19**, 1–15
1204 (2018).
1205 91. Saelens, W., Cannoodt, R., Todorov, H. & Saeys, Y. A comparison of single-cell trajectory
1206 inference methods. *Nat. Biotechnol.* **37**, 547–554 (2019).
1207 92. Street, K. *et al.* Slingshot: cell lineage and pseudotime inference for single-cell
1208 transcriptomics. *BMC Genomics* **19**, 1–16 (2018).
1209 93. Fisher, R. A. Statistical Methods for Research Workers. *Breakthroughs in Statistics* 66–70
1210 (1992).
1211 94. Benjamini, Y. & Hochberg, Y. Controlling the False Discovery Rate: A Practical and Powerful
1212 Approach to Multiple Testing. *J. R. Stat. Soc. Series B Stat. Methodol.* **57**, 289–300 (1995).
1213 95. Zhang, B. & Horvath, S. A General Framework for Weighted Gene Co-Expression Network
1214 Analysis. *Stat. Appl. Genet. Mol. Biol.* **4**, (2005).
1215 96. Stoica, P. & Selen, Y. Model-order selection: a review of information criterion rules.
1216 https://ieeexplore.ieee.org/document/1311138.
1217 97. Alvarez, M. J. *et al.* Network-based inference of protein activity helps functionalize the genetic
1218 landscape of cancer. *Nat. Genet.* **48**, 838 (2016).
1219 98. Müller-Dott, S. *et al.* Expanding the coverage of regulons from high-confidence prior
1220 knowledge for accurate estimation of transcription factor activities. *Nucleic Acids Res* **51**,

10934–10949 (2023).
99. Akhmedov, M. *et al.* PCSF: An R-package for network-based interpretation of high-throughput data. *PLoS Comput. Biol.* **13**, e1005694 (2017).
100. Kuleshov, M. V. *et al.* Enrichr: a comprehensive gene set enrichment analysis web server 2016 update. *Nucleic Acids Res.* **44**, W90–W97 (2016).
101. Lachmann, A. *et al.* ChEA: transcription factor regulation inferred from integrating genome-wide ChIP-X experiments. *Bioinformatics* **26**, 2438–2444 (2010).
102. Stormo, G. D. Modeling the specificity of protein-DNA interactions. *Quantitative Biology* **1**, 115–130 (2013).
103. Wasserman, W. W. & Sandelin, A. Applied bioinformatics for the identification of regulatory elements. *Nat. Rev. Genet.* **5**, 276–287 (2004).
104. Gillespie, M. *et al.* The reactome pathway knowledgebase 2022. *Nucleic Acids Res.* **50**, D687–D692 (2021).
105. Kanehisa, M. & Goto, S. KEGG: kyoto encyclopedia of genes and genomes. *Nucleic Acids Res.* **28**, (2000).
106. Wrzodek, C., Büchel, F., Ruff, M., Dräger, A. & Zell, A. Precise generation of systems biology models from KEGG pathways. *BMC Syst. Biol.* **7**, (2013).
107. Romero, P. *et al.* Computational prediction of human metabolic pathways from the complete human genome. *Genome Biol.* **6**, (2005).
108. Thiele, I. *et al.* A community-driven global reconstruction of human metabolism. *Nat. Biotechnol.* **31**, (2013).
109. Rodchenkov, I. *et al.* Pathway Commons 2019 Update: integration, analysis and exploration of pathway data. *Nucleic Acids Res.* **48**, D489–D497 (2019).
110. Türei, D., Korcsmáros, T. & Saez-Rodriguez, J. OmniPath: guidelines and gateway for literature-curated signaling pathway resources. *Nat. Methods* **13**, 966–967 (2016).
111. Türei, D. *et al.* Integrated intra- and intercellular signaling knowledge for multicellular omics analysis. *Mol. Syst. Biol.* **17**, e9923 (2021).
112. OmnipathR. *Bioconductor* http://bioconductor.org/packages/OmnipathR/.
113. Csárdi, G. *et al.* Igraph: Network analysis and visualization. *CRAN: Contributed Packages* The R Foundation https://doi.org/10.32614/cran.package.igraph (2006).
114. Aleksander, S. A. *et al.* The Gene Ontology knowledgebase in 2023. *Genetics* **224**, (2023).
115. Yu, G. *et al.* GOSemSim: an R package for measuring semantic similarity among GO terms and gene products. *Bioinformatics* **26**, 976–978 (2010).

116. Resnik, P. Semantic Similarity in a Taxonomy: An Information-Based Measure and its Application to Problems of Ambiguity in Natural Language. *jair* **11**, 95–130 (1999).
117. An Information-Theoretic Definition of Similarity. https://dl.acm.org/doi/10.5555/645527.657297 doi:10.5555/645527.657297.
118. Wang, J. Z., Du, Z., Payattakool, R., Yu, P. S. & Chen, C.-F. A new method to measure the semantic similarity of GO terms. *Bioinformatics* **23**, 1274–1281 (2007).
119. Charmpi, K., Chokkalingam, M., Johnen, R. & Beyer, A. Optimizing network propagation for multi-omics data integration. *PLoS Comput. Biol.* **17**, e1009161 (2021).
120. En masse organoid phenotyping informs metabolic-associated genetic susceptibility to NASH. *Cell* **185**, 4216–4232.e16 (2022).
121. Graupera, I. *et al.* LiverScreen project: study protocol for screening for liver fibrosis in the general population in European countries. *BMC Public Health* **22**, 1–10 (2022).
122. Hendriks, D. *et al.* Engineered human hepatocyte organoids enable CRISPR-based target discovery and drug screening for steatosis. *Nat. Biotechnol.* **41**, 1567–1581 (2023).
123. Lee, E., Korf, H. & Vidal-Puig, A. An adipocentric perspective on the development and progression of non-alcoholic fatty liver disease. *Journal of hepatology* **78**, (2023).
124. A network-based computational and experimental framework for repurposing compounds toward the treatment of non-alcoholic fatty liver disease. *iScience* **25**, 103890 (2022).
125. Love, M. I., Huber, W. & Anders, S. Moderated estimation of fold change and dispersion for RNA-seq data with DESeq2. *Genome Biol.* **15**, 1–21 (2014).
126. The anatomy of a large-scale hypertextual Web search engine. *Computer Networks and ISDN Systems* **30**, 107–117 (1998).
127. Measure the semantic similarity of GO terms using aggregate information content. *IEEE/ACM Transactions on Computational Biology and Bioinformatics (TCBB)* (2014) doi:10.1109/TCBB.2013.176.
128. Hao, Y. *et al.* Dictionary learning for integrative, multimodal and scalable single-cell analysis. *Nature Biotechnology* **42**, 293–304 (2023).
129. Vathrakokoili, P. A. *et al.* CATD: a reproducible pipeline for selecting cell-type deconvolution methods across tissues. *Bioinformatics advances* **4**, (2024).
130. Zheng, S. C. *et al.* EpiDISH web server: Epigenetic Dissection of Intra-Sample-Heterogeneity with online GUI. *Bioinformatics (Oxford, England)* **36**, (2019).
131. Baron, M. *et al.* A Single-Cell Transcriptomic Map of the Human and Mouse Pancreas Reveals Inter- and Intra-cell Population Structure. *Cell systems* **3**, (2016).

1287 132. Tsoucas, D. *et al.* Accurate estimation of cell-type composition from gene expression data.
1288 *Nature Communications* **10**, 1–9 (2019).
1289 133. Newman, A. M. *et al.* Robust enumeration of cell subsets from tissue expression profiles.
1290 *Nature Methods* **12**, 453–457 (2015).
1291 134. Hao, Y., Yan, M., Heath, B. R., Lei, Y. L. & Xie, Y. Fast and robust deconvolution of tumor
1292 infiltrating lymphocyte from expression profiles using least trimmed squares. *PLoS*
1293 *computational biology* **15**, (2019).
1294 135. Chu, T., Wang, Z., Pe'er, D. & Danko, C. G. Cell type and gene expression deconvolution
1295 with BayesPrism enables Bayesian integrative analysis across bulk and single-cell RNA
1296 sequencing in oncology. *Nature Cancer* **3**, 505–517 (2022).
1297 136. Satija, R., Farrell, J. A., Gennert, D., Schier, A. F. & Regev, A. Spatial reconstruction of single-
1298 cell gene expression data. *Nature Biotechnology* **33**, 495–502 (2015).
1299 137. Mendez, D. *et al.* ChEMBL: towards direct deposition of bioassay data. *Nucleic acids*
1300 *research* **47**, (2019).
1301 138. Yilmaz, Y. & Eren, F. Serum biomarkers of fibrosis and extracellular matrix remodeling in
1302 patients with nonalcoholic fatty liver disease: association with liver histology. *European*
1303 *journal of gastroenterology & hepatology* **31**, (2019).
1304 139. Coilly, A., Desterke, C., Guettier, C., Samuel, D. & Chiappini, F. FABP4 and MMP9 levels
1305 identified as predictive factors for poor prognosis in patients with nonalcoholic fatty liver using
1306 data mining approaches and gene expression analysis. *Scientific reports* **9**, (2019).
1307 140. Toyoda, H. *et al.* Higher hepatic gene expression and serum levels of matrix
1308 metalloproteinase-2 are associated with steatohepatitis in non-alcoholic fatty liver diseases.
1309 *Biomarkers : biochemical indicators of exposure, response, and susceptibility to chemicals*
1310 **18**, (2013).
1311 141. Qi, S., Wang, C., Li, C., Wang, P. & Liu, M. Candidate genes investigation for severe
1312 nonalcoholic fatty liver disease based on bioinformatics analysis. *Medicine* **96**, (2017).

1313

1314 ## Figure Legends

1315 **Figure 1. Pseudo-temporal ordering of patients captures disease progression and**
1316 **identifies MASLD gene signature. A.** Schematic of pseudotemporal ordering of patients based
1317 on bulk transcriptomics data from liver biopsies and stratification of patients into sliding windows.
1318 **B.** Pseudo-temporal ordering of patients based on transcriptomic data recapitulates disease
1319 progression based on individual phenotypes, i.e., steatosis, ballooning, inflammation and fibrosis,
1320 and based on the NAS and MASLD scores. **C-D.** Pseudotemporal ordering of two independent
1321 orthogonal datasets, based on the 145 genes that are most predictive of the trajectory, provides
1322 a linear and clear separation of the disease stages (EPoS dataset (**C**) and Gubra dataset (**D**)).
1323 Triangles show the average position of each histopathologically characterised stage on the
1324 trajectory. **E.** Functional enrichment analysis results of these 145 genes using EnrichR, where the
1325 Combined Score (c) has been calculated as c = log(p_value) * z_score, with p_value representing
1326 the Fisher exact test outcome, and z-score the deviation from the expected rank.

1327 **Figure 2. Phenotype-specific gene modules associated with the different MASLD variables.**
1328 **A.** Schematic of the approach to extract a reference MASLD network. **B.** Association (coefficient
1329 from linear model) of the different gene co-expression modules with NAS score, Steatosis,
1330 Ballooning, and Fibrosis. Red indicates a positive coefficient, whereas blue indicates negative
1331 coefficient. **C.** Heatmap is showing the average scaled expression of the modules along the
1332 pseudotemporal trajectory. The values for each module were calculated by averaging the scores
1333 of SW-grouped samples along its first principal component (eigengene). **D.** TFs whose regulons
1334 are enriched in the modules. The figure shows TFs per module, coloured according to the
1335 adjusted p-value of the enrichment test. The presented TFs have been identified as enriched in
1336 multiple modules. Bold indicates TFs identified as deregulated (FDR<0.05) in at least one sliding
1337 window (see sliding window analysis results). The complete of TFs derived from the enrichment
1338 analysis is given in **Supplementary Table 8. E.** Enrichment of MASLD network and its
1339 components in known MASLD genes curated from the literature (top) or from MSigDB (bottom).

1340 **Figure 3. Sliding window analysis to study the landscape of molecular changes along the**
1341 **MASLD trajectory. A.** Results from TF activity analysis in two types of discrete patient
1342 stratification (Mild, Moderate, Severe and NAS scores), and the pseudotemporal trajectory. The
1343 colour indicates a change in TF activity compared to the previous disease stage. **B.** Mean
1344 phenotype and NAS pathologist scores along the SW trajectory.

1345 **Figure 4. Results of cell type deconvolution analysis. A.** Cell type deconvolution of patient
1346 transcriptomic data along our MASLD trajectory **B.** Prediction of cell types with which the
1347 deregulated processes are associated after excluding gene sets of these processes that could
1348 have been identified as differentiated by the mere change in abundance of cell types.

1349 **Figure 5. Biomarker selection and performance on the external liver transcriptomics and**
1350 **plasma proteomics datasets. A.** Selection of candidate biomarkers. A 57-gene set was defined
1351 by intersecting the global MASLD network with plasma–liver correlated genes[69], followed by
1352 random forest classification of fibrosis stage (F0–2 vs F3–4). Feature importance and the elbow
1353 method identified a reduced 15-gene subset. **B.** Performance of the 57- and 15-gene classifiers
1354 compared with non-invasive clinical scores in the Fujiwara cohort. **C-D.** Benchmarking of the
1355 same models against FIB-4 in the EPoS cohort, with C showing the ROC curve for our model
1356 compared to the FIB-4 score, and D showing the performance using additional metrics. **E.** ROC
1357 curve for fibrosis classification of patients using external plasma proteomics data. **F.** Random
1358 forest regression predicting patient positions along the MASLD trajectory in the Gubra cohort;
1359 predicted positions (57 genes) versus transcriptome-derived positions are shown (R^2, Pearson
1360 correlation). **G-H.** Inferred patient trajectory positions on the external validation plasma
1361 proteomics dataset, using either the whole proteome (G) or only the 57 biomarkers (H). **I.** GWAS
1362 trait enrichment of the 57-gene biomarker panel; significant categories after FDR correction are
1363 shown in orange (Fisher's exact test on the biomarkers associated with each of those categories,
1364 against the whole GWAS as the background).

1365 Supplementary Figure legends

1366 **Supplementary Figure 1. MASLD patients along the continuous transcriptomics-driven**
1367 **trajectory for the internal UCAM/VCU dataset. A.** The colouring is based on the
1368 histopathologists' scores. **B.** Triangles showing the average horizontal position of each scoring
1369 group on the trajectory. Both panels provide information for the NAS score (ranging from 0 to 7),
1370 Steatosis scoring (0-3), Inflammatory damage (0-3), Ballooning (0-2), and Fibrosis (0-4). **C**. Violin
1371 plots illustrate the distribution of the patients in each histopathological scoring group. Each panel
1372 shows the Pearson correlation coefficient (R score) for the mean trajectory positions of each
1373 scoring group. The p-values are the results of ANOVA followed by Tukey's pairwise comparisons
1374 for the distributions of patients across the histopathological scores. The statistically significant
1375 groups are indicated with dashed lines (*p-value < .05, ** p-value < .005, *** p-value < .0005).

1376 **Supplementary Figure 2. Trajectory inference on independent MASLD transcriptomic**
1377 **datasets and MASLD patients along the continuous transcriptomics-driven trajectory for**
1378 **the external longitudinal (Fujiwara) dataset. A.** Trajectory inference for the independent EPoS
1379 dataset using the whole transcriptome. Color coding depicts MASLD stages as published with the
1380 original RNA-Seq data. Triangles show the average horizontal position of each scoring group on
1381 the trajectory. **B.** Trajectory inference for the independent GUBRA dataset. The population was
1382 characterised as Healthy (non-obese individuals without MASLD/MASH), Obese (healthy but
1383 obese individuals without MASLD/MASH), MASL, and MASH. **C.** Fujiwara dataset: Patient
1384 movement on the trajectory between the two biopsies. Movement towards the left or right
1385 indicates disease regression or progression, respectively. The colour shows the change in NAS
1386 score between the two biopsies, with positive scores indicating an increase in the second biopsy.
1387 **D.** Overview of patients' positions shift on the trajectory by the NAS change between the two
1388 biopsies. Statistical significance between the patients' position change for the increased and
1389 decreased NAS score was calculated using the Wilcoxon test. **E.** Similar to (D) but for the change
1390 in fibrosis score.

1391 **Supplementary Figure 3. Graph-based approach to find the optimal sequence of sliding**
1392 **windows for the stratification of patients. A.** Generation of a directed acyclic graph, where
1393 each node corresponds to a group of samples (sliding window; SW) aligned by pseudo-temporal
1394 order. Directed edges connect overlapping windows, ensuring continuity along the trajectory. The
1395 graph is generated iteratively until all the samples have been mapped to SW nodes. **B.** Pruning
1396 of the graph to identify candidate SW sequences: differential expression analysis is performed for
1397 each linked pair of SWs on the graph, retaining only edges that meet specific criteria regarding
1398 the number of differentially expressed genes (FDR < 0.1). **C.** The optimal SW sequence is defined
1399 as the one that maximizes the product of three max-scaled criteria: (i) median DEG count, (ii)
1400 number of edges exceeding the lower DEG threshold, and (iii) coefficient of variation of DEG
1401 counts along the path.

1402 **Supplementary Figure 4. Agglomerative clustering of the 57 TFs that were found to be**
1403 **deregulated in two types of discrete patient stratification (Mild, Moderate, Severe and NAS**
1404 **scores), and the pseudotemporal trajectory**. Reactome pathway enrichment analysis was
1405 performed to link TFs to molecular pathways and to create the corresponding one-hot encoding
1406 matrix. The clustering was performed using this matrix to identify groups of functionally related
1407 TFs.

1408 **Supplementary Figure 5. Correlation plots of the activities of TFs for the UCAM/VCU and**
1409 **EPoS datasets**. **A.** Pearson correlation of cumulative activation scores of TFs, which were
1410 identified as deregulated (FDR<0.05) based on the sliding windows analysis in at least one
1411 dataset. **B.** Pearson correlation of the cumulative TF activation scores between the two datasets
1412 for each sliding window. Each dot represents a TF identified as deregulated (FDR<0.05) at least
1413 in one sliding window of a dataset.

1414 **Supplementary Figure 6. Cumulative activation scores of Reactome pathways along the**
1415 **pseudotemporal trajectory.** This list of terms provides a comprehensive description of MASLD-
1416 relevant pathways, derived from the enrichment analysis of deregulated network signatures along
1417 the disease trajectory and a pruning procedure applied to the hierarchical structure of Reactome.
1418 The SW-based activation score of each pathway was defined as the sum of the activation scores
1419 of its related genes, normalised by the pagerank centralities of these genes within the pathway-
1420 based subnetwork. The respective cumulative scores were defined by progressively summing the
1421 SW-based activation scores.

1422 **Supplementary Figure 7. Correlation plots of the activities of pathways for the UCAM/VCU**
1423 **and EPoS datasets**. **A.** Pearson correlation of cumulative activation scores of Reactome
1424 pathways that were identified as MASLD-relevant, based on the sliding windows analysis in at
1425 least one dataset. **B.** Pearson correlation of cumulative activation scores of Reactome pathways
1426 between the two datasets for each sliding window. Each dot represents a pathway identified as
1427 MASLD-relevant at least in one dataset.

1428 **Supplementary Figure 8. Consensus proportion of cell type along the disease trajectory**.
1429 Cell type deconvolution was applied on the bulk RNA-seq samples using 6 methods. The average
1430 cell type proportions for each sliding window were calculated by averaging the proportions across
1431 the corresponding samples. Finally, the consensus result was calculated as the mean of cell-type
1432 proportion per cell-type across methods.

1433 **Supplementary Figure 9: Performance of the random forest classification and regression**
1434 **models. A.** Performance of model using the 57-biomarker set compared to using random genes.
1435 In both external validation datasets (EPoS and Fujiwara), similar models were run 300 times,
1436 using random 57-gene signatures as input. The red points show our model's AUC for the 57-
1437 biomarker set, while the gray points show the model's performance for the random sets. **B.**
1438 Selection of optimal threshold using Youden's index on the proteomics dataset. **C.** Patient

1439 distributions on the predicted trajectory using the random forest regression model for the internal
1440 UCAM/VCU dataset. Run 1000 times using 5-fold cross validation and the distribution is
1441 generated using the mean result for each patient. Different colors denote different MASLD stages.
1442 Asterisks represent statistical significance after applying ANOVA among the disease stages; * : p
1443 < 0.05, ** : $p < 0.005$, *** : $p < 0.0005$, **** : $p < 0.00005$. **D.** The y-axis shows the positions of
1444 the patients on the "real" trajectory, inferred using the whole transcriptome. The x-axis shows the
1445 predicted positions of patients using only the 57 biomarkers. R^2 denotes the Pearson correlation
1446 score for real vs predicted positions on the trajectory. **E.** Similar to (D) but for the external EPoS
1447 dataset. **F.** Similar to (E) but for random 57-gene signatures. **G.** Results of the random forest
1448 regression model that sorts patients on the MASLD trajectory and performance on the Gubra
1449 dataset (additional validation dataset). Mean squared error for the predicted patients' positions on
1450 the trajectory. The different colours depict the various disease stages (Healthy, Obese, MASL,
1451 MASH). The patients are sorted by their positions along the trajectory, independent of their
1452 relative distances.

1453 **Supplementary Figure 10: Genetic evidence of our 57-biomarker set. A.** Gene-trait category
1454 associations based on the GWAS catalog. Of those, 47/57 biomarkers were associated with at
1455 least one trait (**Supplementary Table 16**), while 13 biomarkers were part of our top 15 biomarker
1456 list (selected using the elbow method). **B.** Number of biomarkers associated with metabolic,
1457 cardiovascular, liver, cancer, neurological or inflammatory traits. Those associated with a different
1458 trait are classified as "other".

1459 **Supplementary Figure 11. Quality control and validation for dataset integration**. **A.** PCA plot
1460 of the merged UCAM/VCU quantile normalised counts. There is an apparent batch effect
1461 separating the patients into two clusters stemming from the dataset from which they are derived.
1462 **B.** COMBAT batch effect correction solved the problem of the batch effect with patients altogether
1463 in a cluster and a clear disease progression pattern from the right towards the later disease stages
1464 on the left. The outlier (sample 5) was removed from all downstream analyses. **C-D.** Normalised
1465 counts before and after batch effect correction, separately for each disease stage. The data
1466 suggest that COMBAT has not significantly altered gene expression, as indicated by the high
1467 correlation ($R > 0.97$) across all MASLD stages in the VCU (C) and UCAM (D) datasets. Inset in
1468 panel D shows the mean correlation in expression before and after correction stratified by low,
1469 medium, and high expression levels. The categories were defined by ranking genes by
1470 normalised expression in each stage and dividing them into three groups (High: top third, Medium:

1471 middle third, and Low: bottom third). The dots inside each bar correspond to the correlations of
1472 expression separately for each disease stage (dot colours in agreement with disease stage
1473 colours from panel C). **E.** Correlation of the principal components (PCs) with the variables of
1474 interest. The first 10 PCs have been correlated using Pearson correlation with 6 continuous
1475 variables of interest: age, NAS score, Fibrosis, Steatosis, Ballooning, and Inflammation. **F.**
1476 Heatmap of the quantile normalised counts before and after the merging/batch effect correction
1477 for UCAM and VCU datasets. The rows show genes previously linked to MASLD[138–141]. The data
1478 are shown in a "fold change vs the first disease stage" of each dataset, respectively ("red" =
1479 increase; "blue" = decrease; "white" = unchanged; "green datasets": UCAM and VCU before
1480 correction; "blue datasets": UCAM and VCU after correction; the asterisks "*" in the column names
1481 indicate that the samples have been batch-effect corrected). Note that the control group (the first
1482 column in each block) in the VCU dataset is labelled as CTRL, while in the UCAM it is labelled as
1483 MASL.

1484 Supplementary Table legends

1485 **Supplementary Table 1.** Information about all MASLD patients used in this study (UCAM and
1486 VCU datasets). For each patient we provide the histopathology score (steatosis, ballooning,
1487 inflammation, fibrosis, NAS score) and the MASLD stage, as well as additional metadata (age,
1488 sex), the Sliding Window (SW) number assigned to the patient, the order in the trajectory (1 to
1489 136), the position according to PC1, the dataset (UCAM or VCU), the batch corrected normalised
1490 expression value per gene, and whether or not the gene is present in the gene panels we identify
1491 in this study (145 trajectory inference gene set, 57 or 15 biomarker panel).

1492 **Supplementary Table 2.** Patients' clinical characteristics when divided into CTRL, MASL, MASH
1493 F0-1, MASH F2, MASH F3-4. Statistical significance is assessed by ANOVA. The letters next to
1494 the values indicate post-hoc analysis significance based on Tukey's test; "[a]" means reference
1495 group; when groups show different letters, they should be considered statistically different at the
1496 post-hoc comparison; groups showing the same letter are statistically not-significant at the post-
1497 hoc comparison.

1498 **Supplementary Table 3.** Random forest's accuracy and AUC, tested on UCAM/VCU and
1499 GUBRA datasets, using the top 145 genes. The UCAM/VCU dataset has been split into training
1500 (80%), and test (20%) sets, and the metrics given in the table are the average over 1000 test-set

1501 runs. The gene signature predicts the different MASLD characteristics (Steatosis, Inflammation,
1502 Ballooning, Fibrosis) and the MASLD stage. For the GUBRA dataset predictions, the whole
1503 UCAM/VCU dataset has been used as a training set. The only available information for this
1504 external dataset is the MASLD stage. Finally, for both datasets, a random set of 20, 145, and
1505 5000 genes (averaged across 1000 runs) verifies the robustness of the selected genes.

1506 **Supplementary Table 4.** Pathway enrichment analysis of the 145 genes identified by random
1507 forest as key contributors to defining the MASLD disease trajectory.

1508 **Supplementary Table 5.** Patient assignment to each of the 13 Sliding Windows (SWs).

1509 **Supplementary Table 6.** Genes assigned to each module were identified using WGCNA and
1510 were associated with the histological phenotypes in our dataset.

1511 **Supplementary Table 7.** Reactome pathway enrichment analysis on the filtered gene sets of
1512 each module.

1513 **Supplementary Table 8.** Transcription Factor (TF) enrichment analysis for each significantly-
1514 identified gene module.

1515 **Supplementary Table 9.** Reactome pathways enrichment analysis for each MASLD variable-
1516 based set of TFs.

1517 **Supplementary Table 10.** Unified inferred global MASLD network according to our analysis. The
1518 file includes both the UCAM/Sanyal and EPoS networks and columns E and F indicate whether
1519 the edge was present in each of these networks.

1520 **Supplementary Table 11.** Literature-curated genes previously associated with MASLD.

1521 **Supplementary Table 12.** VIPER analysis results comparing consecutive Sliding Windows
1522 (SWs). The results are derived from the differentially expressed genes of the previous steps
1523 (Log2FoldChange and p-values). The table is organised into 2-plets showing for each comparison
1524 the FDR and the Normalised Enrichment Score (NES). NES determines whether a TF has
1525 significantly more “activated” than “inhibited” predictions (NES > 0) or vice versa (NES < 0).

1526 **Supplementary Table 13.** Activity scores (cumulative values) of Reactome pathways along the
1527 MASLD trajectory for UCAM/VCU and EPoS datasets.

1528 **Supplementary Table 14**. Consensus estimated cell type proportions per sample in the bulk
1529 RNA-seq dataset.

1530 **Supplementary Table 15.** FDR values from the enrichment analysis between liver cell type
1531 markers and Reactome pathway gene sets, whose differentiation cannot be explained by changes
1532 in cell type composition.

1533 **Supplementary Table 16.** GWAS summary results of gene associations to complex traits

1534 **Supplementary Table 17.** Small molecules extracted from the ChEMBL database as targeting
1535 one of the proteins represented in our 57-protein biomarker panel.

1536 **Supplementary Table 18.** Fujiwara metadata for all patients with paired biopsies. The table
1537 includes Fibrosis scores and NITs (FIB-4, APRI, NFS) scores calculated from the available
1538 metadata.

1539 **Supplementary Table 19.** Reference PPI network derived from the integration of multiple
1540 interaction databases: KEGG, ReconX, HumanCyc, Reactome, OmniPath. This network was
1541 used to generate the global MASLD network.

1542 **Supplementary Table 20.** Slim version of the Reactome database. The hierarchical graph has
1543 been pruned using the Information Content (IC) and Semantic Value (SV) properties of terms,
1544 retaining the most generic ones. Two columns indicate if a term has been included in the MASLD-
1545 related subgraphs of the UCAM-VCU and EpoS datasets

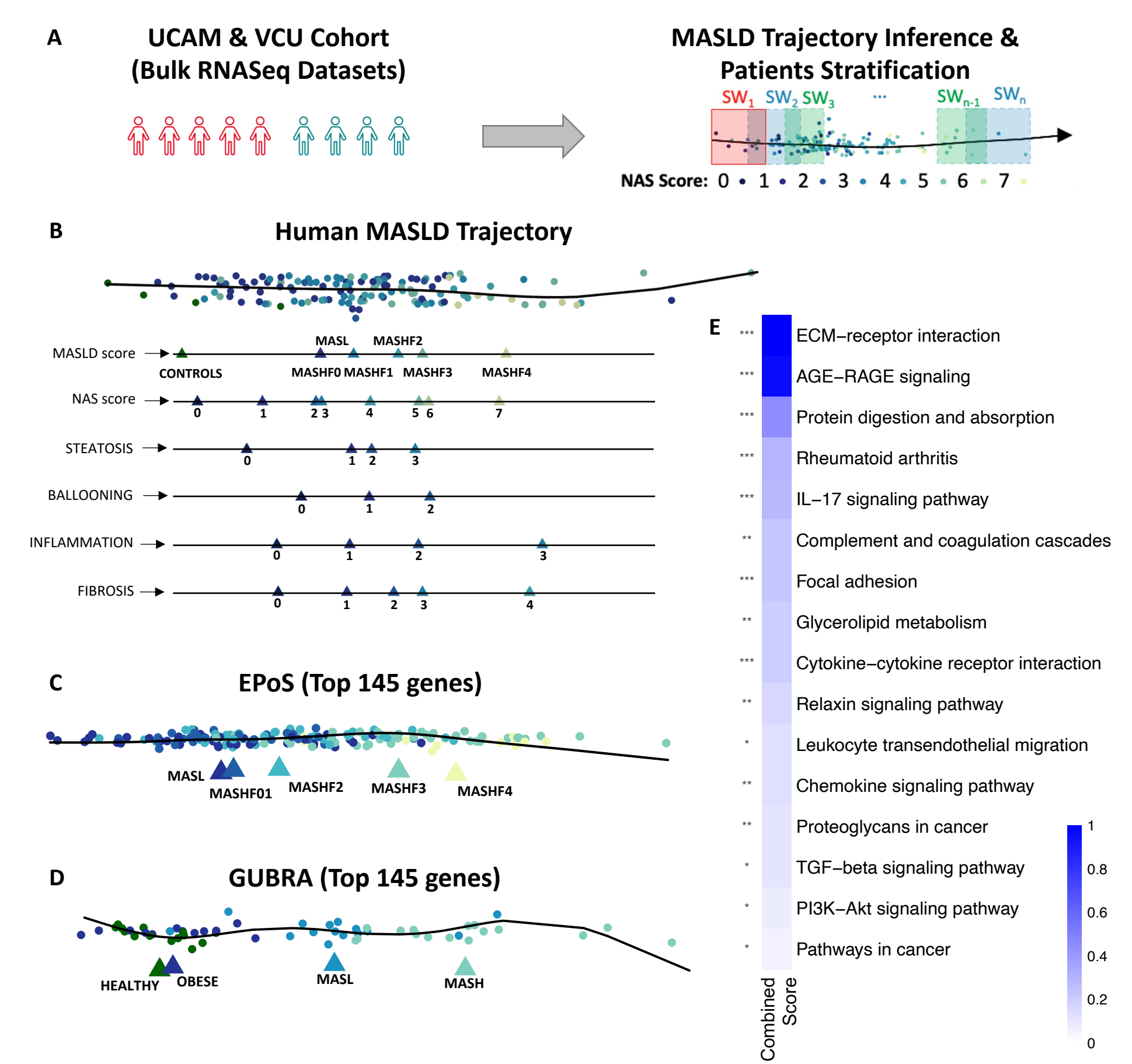
A
UCAM & VCU Cohort
(Bulk RNASeq Datasets)
MASLD Trajectory Inference &
Patients Stratification
SW1 SW2 SW3 ... SWn-1 SWn
NAS Score: 0 1 2 3 4 5 6 7
B
Human MASLD Trajectory
MASLD score
CONTROLS
MASL
MASHF0 MASHF1
MASHF2
MASHF3
MASHF4
NAS score
0 1 2 3 4 5 6 7
STEATOSIS
0 1 2 3
BALLOONING
0 1 2
INFLAMMATION
0 1 2 3
FIBROSIS
0 1 2 3 4
C
EPoS (Top 145 genes)
MASL
MASHF01
MASHF2
MASHF3
MASHF4
D
GUBRA (Top 145 genes)
HEALTHY
OBESE
MASL
MASH
E
*** ECM−receptor interaction
*** AGE−RAGE signaling
*** Protein digestion and absorption
*** Rheumatoid arthritis
*** IL−17 signaling pathway
** Complement and coagulation cascades
*** Focal adhesion
** Glycerolipid metabolism
*** Cytokine−cytokine receptor interaction
** Relaxin signaling pathway
* Leukocyte transendothelial migration
** Chemokine signaling pathway
** Proteoglycans in cancer
* TGF−beta signaling pathway
* PI3K−Akt signaling pathway
* Pathways in cancer
Combined Score
1
0.8
0.6
0.4
0.2
0

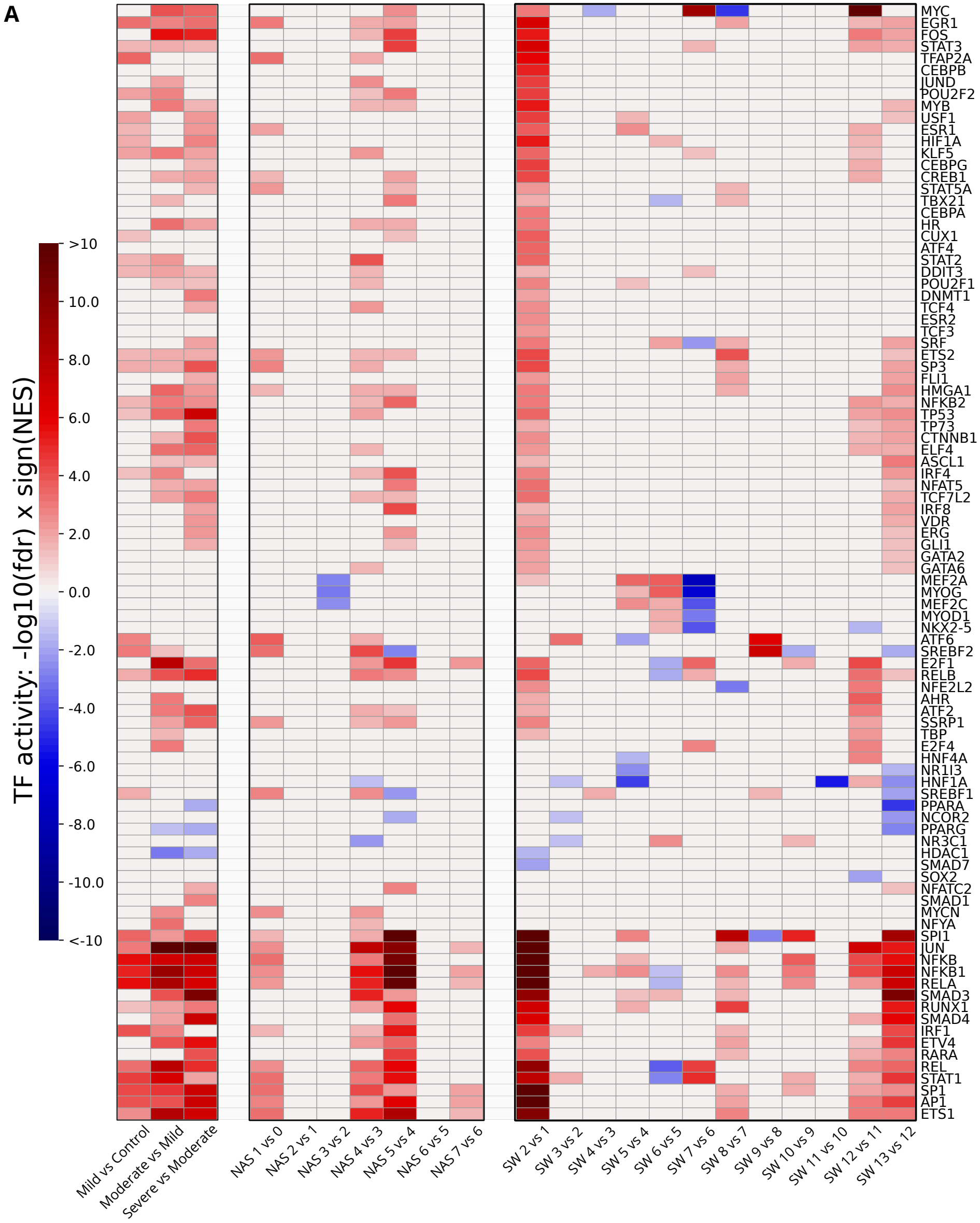
A
TF activity: -log10(fdr) x sign(NES)
>10
10.0
8.0
6.0
4.0
2.0
0.0
-2.0
-4.0
-6.0
-8.0
-10.0
<-10
MYC
EGR1
FOS
STAT3
TFAP2A
CEBPB
JUND
POU2F2
MYB
USF1
ESR1
HIF1A
KLF5
CEBPG
CREB1
STAT5A
TBX21
CEBPA
HR
CUX1
ATF4
STAT2
DDIT3
POU2F1
DNMT1
TCF4
ESR2
TCF3
SRF
ETS2
SP3
FLI1
HMGA1
NFKB2
TP53
TP73
CTNNB1
ELF4
ASCL1
IRF4
NFAT5
TCF7L2
IRF8
VDR
ERG
GLI1
GATA2
GATA6
MEF2A
MYOG
MEF2C
MYOD1
NKX2-5
ATF6
SREBF2
E2F1
RELB
NFE2L2
AHR
ATF2
SSRP1
TBP
E2F4
HNF4A
NR1I3
HNF1A
SREBF1
PPARA
NCOR2
PPARG
NR3C1
HDAC1
SMAD7
SOX2
NFATC2
SMAD1
MYCN
NFYA
SPI1
JUN
NFKB
NFKB1
RELA
SMAD3
RUNX1
SMAD4
IRF1
ETV4
RARA
REL
STAT1
SP1
AP1
ETS1
Mild vs Control
Moderate vs Mild
Severe vs Moderate
NAS 1 vs 0
NAS 2 vs 1
NAS 3 vs 2
NAS 4 vs 3
NAS 5 vs 4
NAS 6 vs 5
NAS 7 vs 6
SW 2 vs 1
SW 3 vs 2
SW 4 vs 3
SW 5 vs 4
SW 6 vs 5
SW 7 vs 6
SW 8 vs 7
SW 9 vs 8
SW 10 vs 9
SW 11 vs 10
SW 12 vs 11
SW 13 vs 12

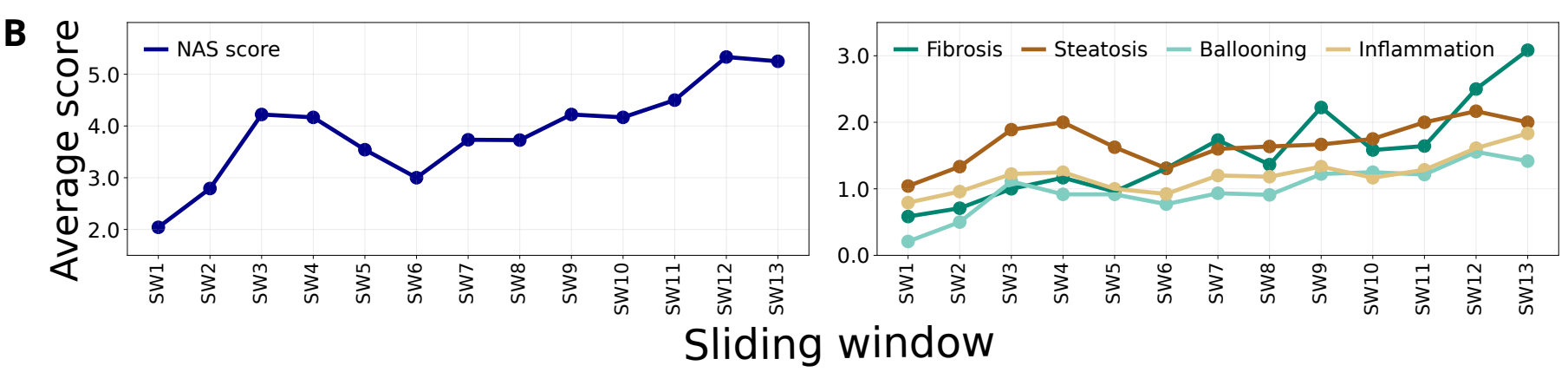
B
Average score
NAS score
5.0
4.0
3.0
2.0
Fibrosis
Steatosis
Ballooning
Inflammation
3.0
2.0
1.0
0.0
SW1
SW2
SW3
SW4
SW5
SW6
SW7
SW8
SW9
SW10
SW11
SW12
SW13
Sliding window

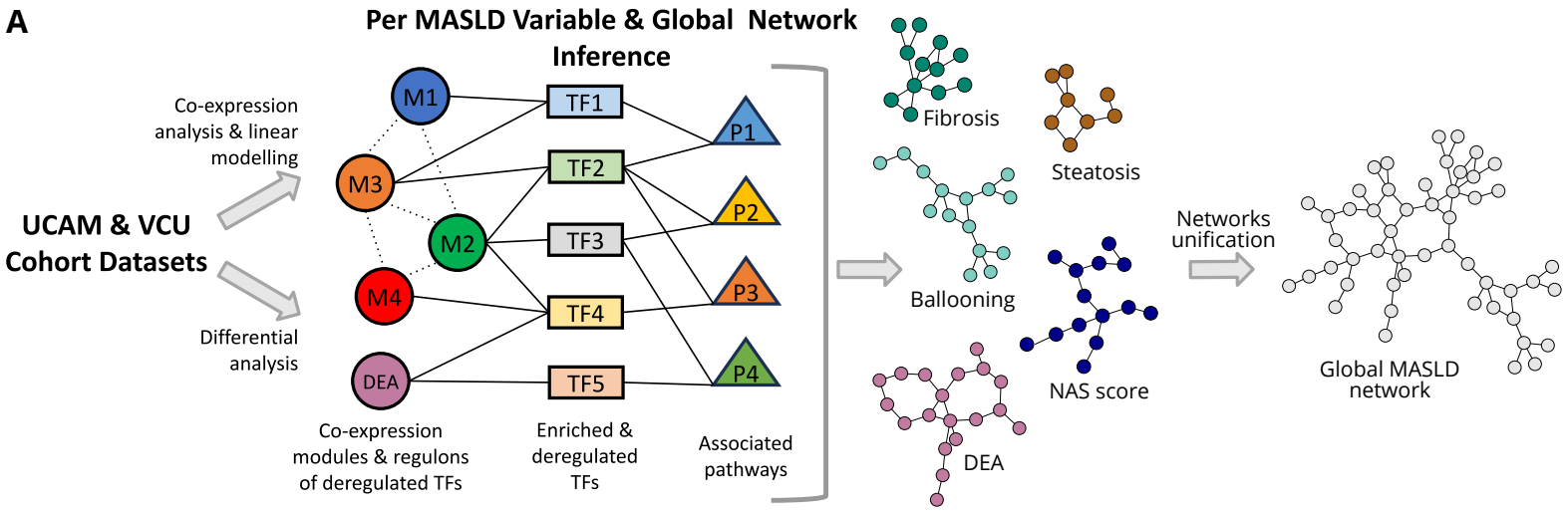
A
Per MASLD Variable & Global Network Inference
UCAM & VCU Cohort Datasets
Co-expression analysis & linear modelling
Differential analysis
M1
M2
M3
M4
DEA
TF1
TF2
TF3
TF4
TF5
P1
P2
P3
P4
Co-expression modules & regulons of deregulated TFs
Enriched & deregulated TFs
Associated pathways
Fibrosis
Steatosis
Ballooning
NAS score
DEA
Networks unification
Global MASLD network

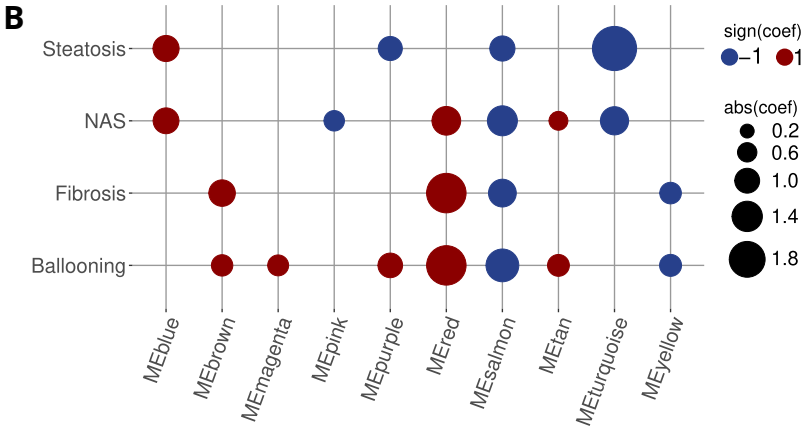
B
Steatosis
NAS
Fibrosis
Ballooning
MEblue
MEbrown
MEmagenta
MEpink
MEpurple
MEred
MEsalmon
MEtan
MEturquoise
MEyellow
sign(coef)
−1
1
abs(coef)
0.2
0.6
1.0
1.4
1.8

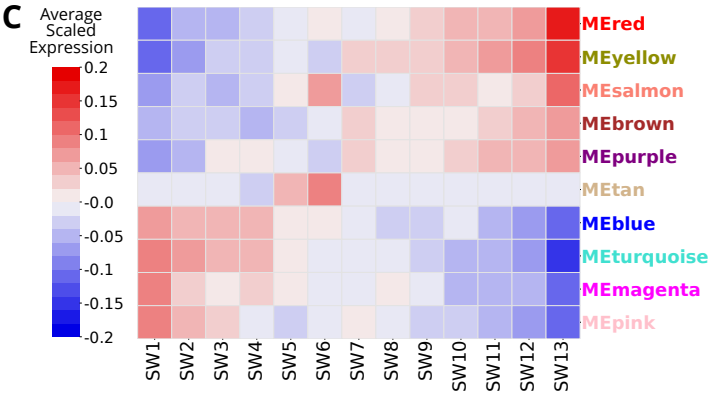
C
Average Scaled Expression
0.2
0.15
0.1
0.05
0.0
-0.05
-0.1
-0.15
-0.2
MEred
MEyellow
MEsalmon
MEbrown
MEpurple
MEtan
MEblue
MEturquoise
MEmagenta
MEpink
SW1
SW2
SW3
SW4
SW5
SW6
SW7
SW8
SW9
SW10
SW11
SW12
SW13

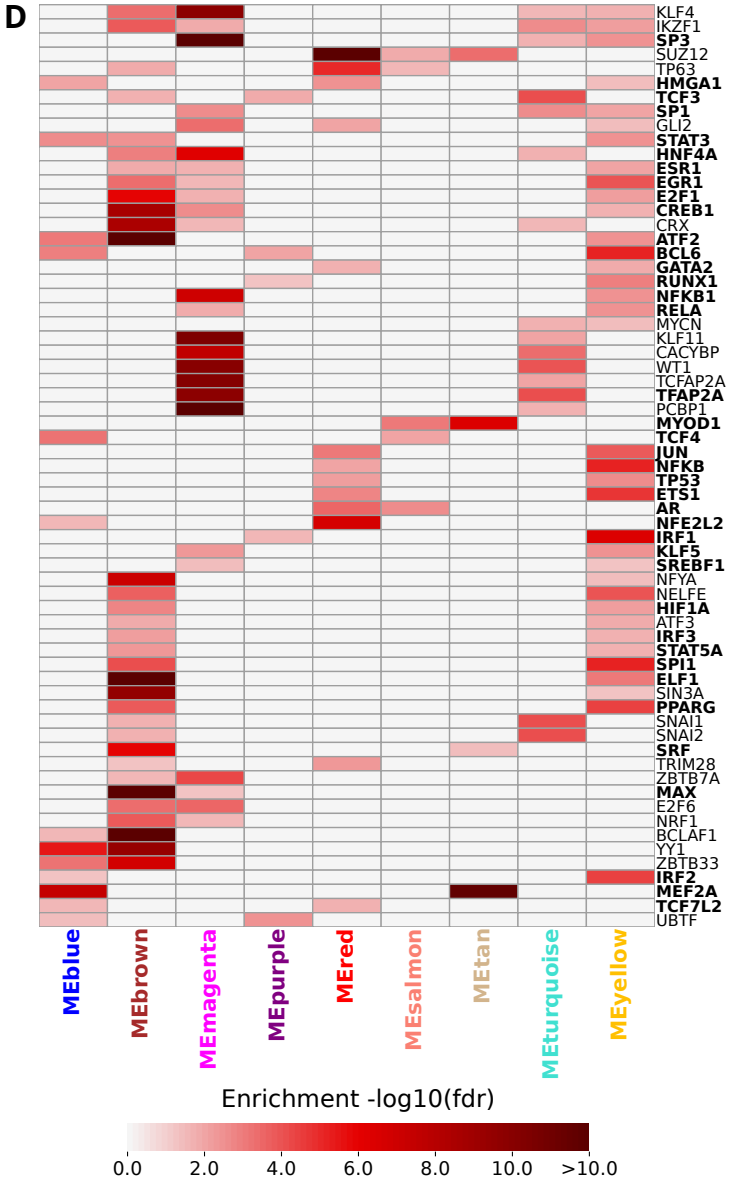
D
KLF4
IKZF1
SP3
SUZ12
TP63
HMGA1
TCF3
SP1
GLI2
STAT3
HNF4A
ESR1
EGR1
E2F1
CREB1
CRX
ATF2
BCL6
GATA2
RUNX1
NFKB1
RELA
MYCN
KLF11
CACYBP
WT1
TCFAP2A
TFAP2A
PCBP1
MYOD1
TCF4
JUN
NFKB
TP53
ETS1
AR
NFE2L2
IRF1
KLF5
SREBF1
NFYA
NELFE
HIF1A
ATF3
IRF3
STAT5A
SPI1
ELF1
SIN3A
PPARG
SNAI1
SNAI2
SRF
TRIM28
ZBTB7A
MAX
E2F6
NRF1
BCLAF1
YY1
ZBTB33
IRF2
MEF2A
TCF7L2
UBTF
MEblue
MEbrown
MEmagenta
MEpurple
MEred
MEsalmon
MEtan
MEturquoise
MEyellow
Enrichment -log10(fdr)
0.0
2.0
4.0
6.0
8.0
10.0
>10.0

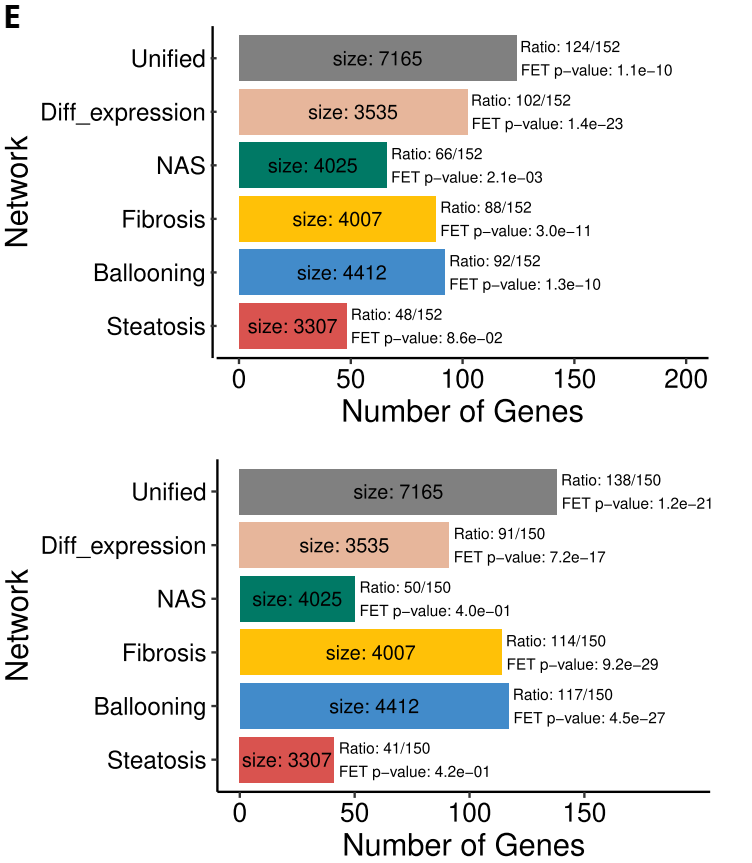
E
Network
Unified
size: 7165
Ratio: 124/152
FET p-value: 1.1e−10
Diff_expression
size: 3535
Ratio: 102/152
FET p-value: 1.4e−23
NAS
size: 4025
Ratio: 66/152
FET p-value: 2.1e−03
Fibrosis
size: 4007
Ratio: 88/152
FET p-value: 3.0e−11
Ballooning
size: 4412
Ratio: 92/152
FET p-value: 1.3e−10
Steatosis
size: 3307
Ratio: 48/152
FET p-value: 8.6e−02
0
50
100
150
200
Number of Genes
Network
Unified
size: 7165
Ratio: 138/150
FET p-value: 1.2e−21
Diff_expression
size: 3535
Ratio: 91/150
FET p-value: 7.2e−17
NAS
size: 4025
Ratio: 50/150
FET p-value: 4.0e−01
Fibrosis
size: 4007
Ratio: 114/150
FET p-value: 9.2e−29
Ballooning
size: 4412
Ratio: 117/150
FET p-value: 4.5e−27
Steatosis
size: 3307
Ratio: 41/150
FET p-value: 4.2e−01
0
50
100
150
Number of Genes

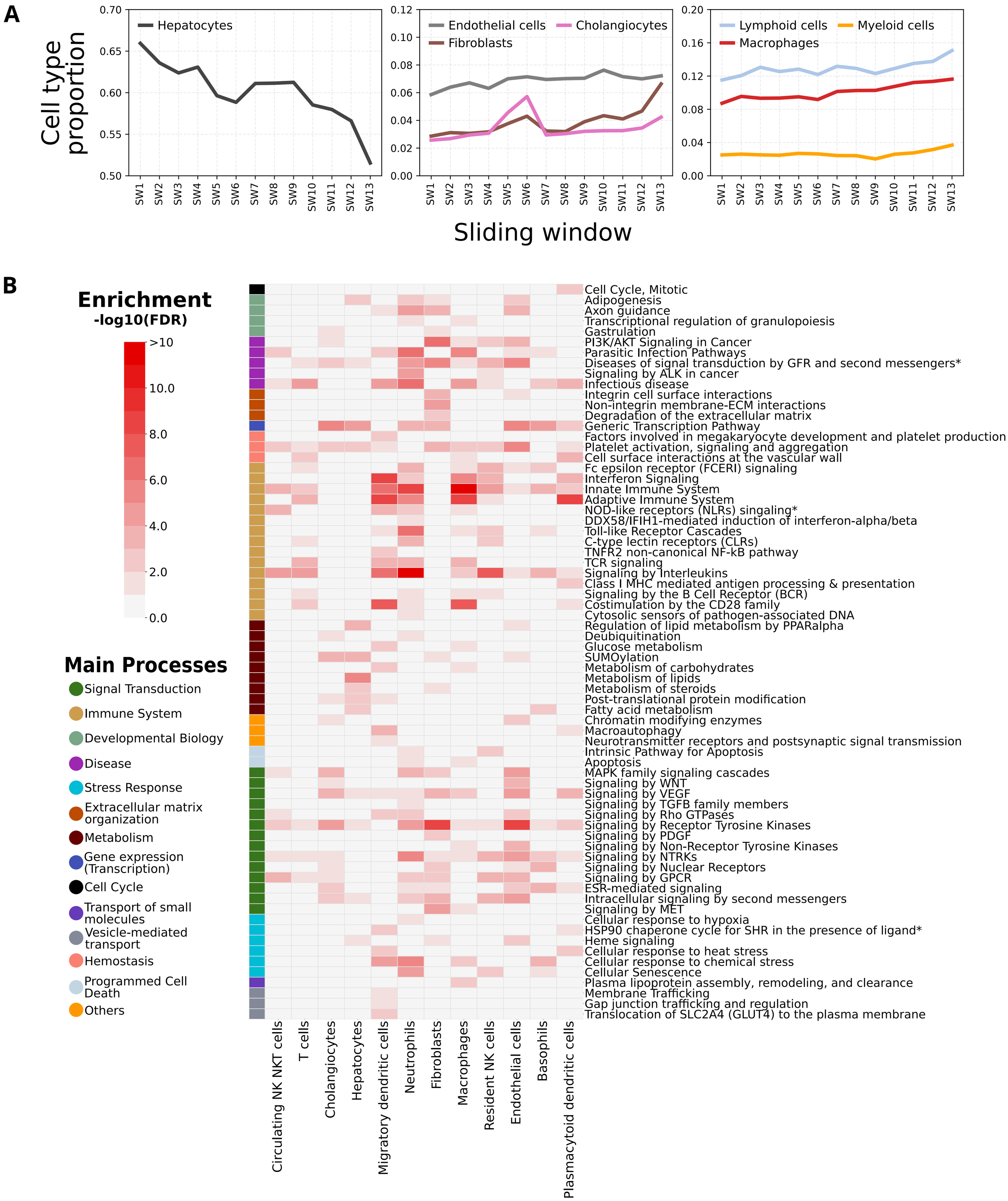
A
Cell type proportion
Hepatocytes
Endothelial cells
Cholangiocytes
Fibroblasts
Lymphoid cells
Myeloid cells
Macrophages
SW1 SW2 SW3 SW4 SW5 SW6 SW7 SW8 SW9 SW10 SW11 SW12 SW13
Sliding window
B
Enrichment
-log10(FDR)
>10
10.0
8.0
6.0
4.0
2.0
0.0
Main Processes
Signal Transduction
Immune System
Developmental Biology
Disease
Stress Response
Extracellular matrix organization
Metabolism
Gene expression (Transcription)
Cell Cycle
Transport of small molecules
Vesicle-mediated transport
Hemostasis
Programmed Cell Death
Others
Cell Cycle, Mitotic
Adipogenesis
Axon guidance
Transcriptional regulation of granulopoiesis
Gastrulation
PI3K/AKT Signaling in Cancer
Parasitic Infection Pathways
Diseases of signal transduction by GFR and second messengers*
Signaling by ALK in cancer
Infectious disease
Integrin cell surface interactions
Non-integrin membrane-ECM interactions
Degradation of the extracellular matrix
Generic Transcription Pathway
Factors involved in megakaryocyte development and platelet production
Platelet activation, signaling and aggregation
Cell surface interactions at the vascular wall
Fc epsilon receptor (FCERI) signaling
Interferon Signaling
Innate Immune System
Adaptive Immune System
NOD-like receptors (NLRs) singaling*
DDX58/IFIH1-mediated induction of interferon-alpha/beta
Toll-like Receptor Cascades
C-type lectin receptors (CLRs)
TNFR2 non-canonical NF-kB pathway
TCR signaling
Signaling by Interleukins
Class I MHC mediated antigen processing & presentation
Signaling by the B Cell Receptor (BCR)
Costimulation by the CD28 family
Cytosolic sensors of pathogen-associated DNA
Regulation of lipid metabolism by PPARalpha
Deubiquitination
Glucose metabolism
SUMOylation
Metabolism of carbohydrates
Metabolism of lipids
Metabolism of steroids
Post-translational protein modification
Fatty acid metabolism
Chromatin modifying enzymes
Macroautophagy
Neurotransmitter receptors and postsynaptic signal transmission
Intrinsic Pathway for Apoptosis
Apoptosis
MAPK family signaling cascades
Signaling by WNT
Signaling by VEGF
Signaling by TGFB family members
Signaling by Rho GTPases
Signaling by Receptor Tyrosine Kinases
Signaling by PDGF
Signaling by Non-Receptor Tyrosine Kinases
Signaling by NTRKs
Signaling by Nuclear Receptors
Signaling by GPCR
ESR-mediated signaling
Intracellular signaling by second messengers
Signaling by MET
Cellular response to hypoxia
HSP90 chaperone cycle for SHR in the presence of ligand*
Heme signaling
Cellular response to heat stress
Cellular response to chemical stress
Cellular Senescence
Plasma lipoprotein assembly, remodeling, and clearance
Membrane Trafficking
Gap junction trafficking and regulation
Translocation of SLC2A4 (GLUT4) to the plasma membrane
Circulating NK NKT cells
T cells
Cholangiocytes
Hepatocytes
Migratory dendritic cells
Neutrophils
Fibroblasts
Macrophages
Resident NK cells
Endothelial cells
Basophils
Plasmacytoid dendritic cells

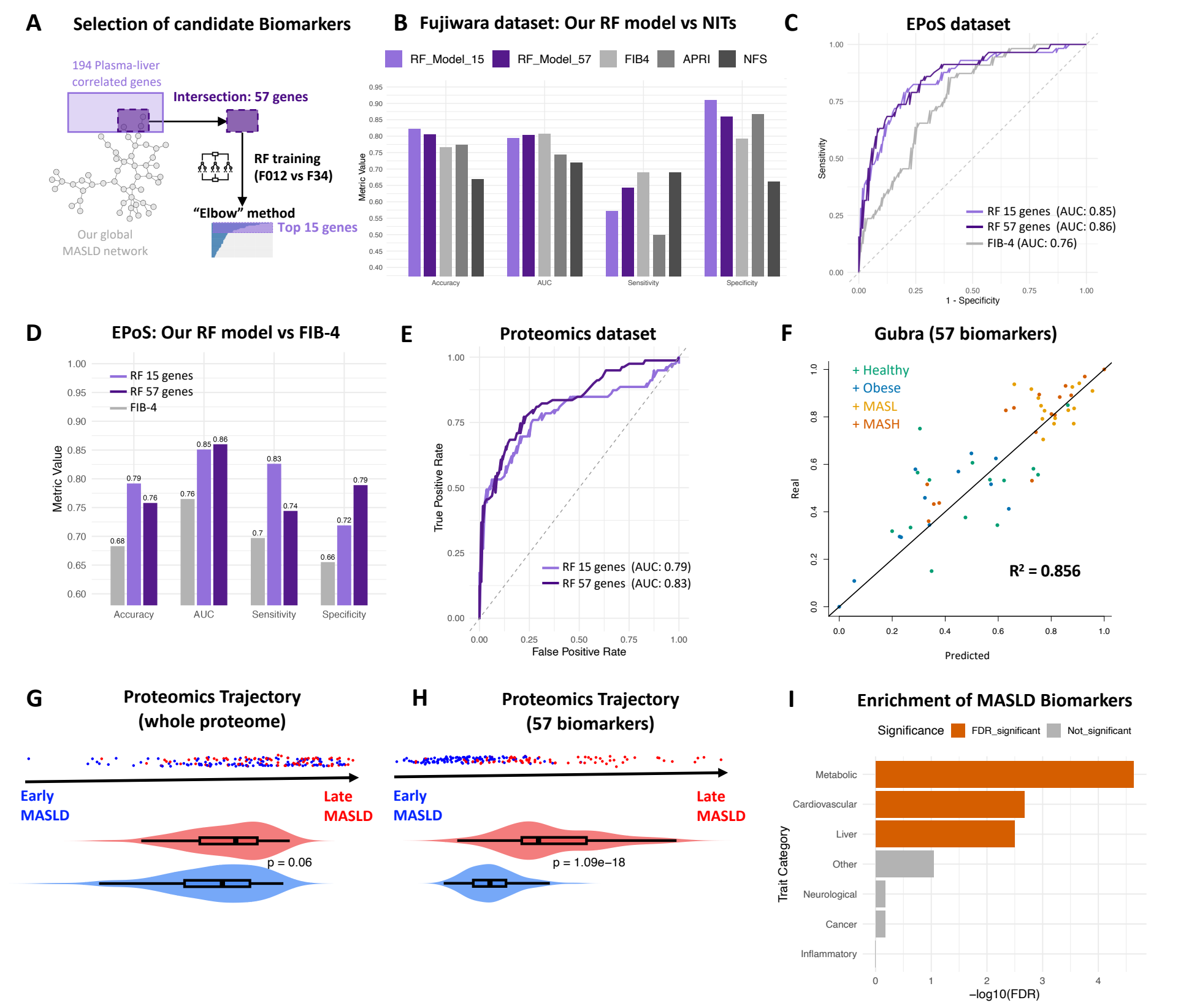
A
Selection of candidate Biomarkers
194 Plasma-liver correlated genes
Intersection: 57 genes
RF training (F012 vs F34)
"Elbow" method
Top 15 genes
Our global MASLD network
B
Fujiwara dataset: Our RF model vs NITs
RF_Model_15
RF_Model_57
FIB4
APRI
NFS
Metric Value
Accuracy
AUC
Sensitivity
Specificity
C
EPoS dataset
Sensitivity
1 - Specificity
RF 15 genes (AUC: 0.85)
RF 57 genes (AUC: 0.86)
FIB-4 (AUC: 0.76)
D
EPoS: Our RF model vs FIB-4
RF 15 genes
RF 57 genes
FIB-4
Metric Value
Accuracy
AUC
Sensitivity
Specificity
E
Proteomics dataset
True Positive Rate
False Positive Rate
RF 15 genes (AUC: 0.79)
RF 57 genes (AUC: 0.83)
F
Gubra (57 biomarkers)
+ Healthy
+ Obese
+ MASL
+ MASH
Real
Predicted
R² = 0.856
G
Proteomics Trajectory (whole proteome)
Early MASLD
Late MASLD
p = 0.06
H
Proteomics Trajectory (57 biomarkers)
Early MASLD
Late MASLD
p = 1.09e−18
I
Enrichment of MASLD Biomarkers
Significance
FDR_significant
Not_significant
Trait Category
Metabolic
Cardiovascular
Liver
Other
Neurological
Cancer
Inflammatory
−log10(FDR)